The study of calcium oxalate kidney stone growth in microfluidic channel

Jiali Wang

Technische Universiteit Delft

TU Delft

The study of calcium oxalate kidney stone growth in microfluidic channel

by

Jiali Wang

to obtain the degree of Master of Science
at the Delft University of Technology,
to be defended publicly on Tuesday August 18, 2020 at 10:00 AM.

Student number:	4514599	
Supervisors:	Dr. Burak Eral	
	Ir. Fatma Ibis	
Thesis committee:	Dr. Burak Eral,	TU Delft, supervisor
	Prof. dr. A. E. D. M. van der Heijden,	TU Delft
	Prof. ir. J. Grievink,	TU Delft

TU Delft

Preface

Kidney stone disease influences 10% of people in the world [36]. Calcium oxalate (CaOx) stones are the most common stones found in the kidney stone. In this research, ANSYS/Fluent CFD was used to determine the supersaturation profile in the microchannel for different constant flow rates and Ca and Ox inlet concentrations. The growth of the CaOx stones is studied by performing experiments in a microfluidic channel under an optical microscopy. The growth of the CaOx stones is also investigated by using a combined transport-kinetics model which couple both mass transport and CaOx precipitation reaction at the surface of the crystal. It is shown that the crystal growth rate increases with solution supersaturation increasing and decreases with the crystal size increasing. The findings also indicated that in cases of low bulk solution supersaturation and low surface reaction constant values, the crystal growth rates are controlled by the surface reaction kinetics and independent on the species transport. When the bulk solution supersaturation and surface reaction constant values are high, the Ca and Ox surface concentrations become lower than the bulk solution concentration values. Thus, the crystal growth rates are controlled by the species transport. The presented study also shows that in the presence of inhibitor osteopontin, the crystal growth rate was decreased.

Jiali Wang
August 2020

Acknowledgements

For the completion of my thesis research, first, I would like to extend my deepest gratitude to my theiss supervisor, Dr. H Burak Eral and daily supervisor, Ir. Fatma Ibis for their constant encouragement, valuable suggestions and enlightening instructions, which contribute to the completion of this thesis.

I am also grateful to Dr. Ir. Herman Kramer, Prof. Dr. Antoine van der Heijden and Dr. Ir. Frederico Marques Phenha for their patient guidance and valuable advice during the weekly meetings.

I would also like to acknowledge my indebtedness to Prof. Ir. J. Grievink who has given me generous support and helpful advice through times of my research.

I am also thankful to the members from the P&E department for their assistance and kindness.

Furthermore, I want to thank my friends for cheering me up and always being there for me.

Last but not least, I owe a lot to my parents, who have given me consistent support and love. I would also like to thank my husband Dezhou Zhang for his support and love.

Jiali Wang

August 2020

Contents

List of Figures

1

Introduction

The background and objectives for research into kidney stone formation are presented in this chapter.

1.1. Kidney stone disease

Kidneys act as filters for the body. The blood is filtered in the tubules of kidneys, removing the waster out of the body. Kidney stone is a hard mass of crystals that are usually formed in the kidneys. The kidney stone disease would not only cause severe pain but also kidney failure in the long term, in addition, 10% of people in the world are suffering this disease [36]. Urine composition consists of different chemicals like calcium, sodium, potassium, oxalate, uric acid and phosphate. These chemicals can clump together and crystallize. The crystals will grow into visible stones in a period of time (weeks to years) which is dependent on reaction condition. Hypercalciuria is one of the reasons that the kidney stones are formed.

The stone size is one of the important characteristics of the kidney stone. Masses less than five millimetres in diameter will usually flush out of the body unforced [7]. When a stone gets larger enough to scratch the walls of the urinary tract, it can cause bleeding and infection or back flow of urine and damage the kidneys. This results in symptoms of nausea, vomiting and a burning sensation while urinating [15].

1.2. Calcium oxalate stone

In 80% kidney stone cases, calcium oxalate CaC_2O_4 (CaOx) is the majority type of kidney stone to form. Calcium oxalate may appear in the form of CaOx monohydrate (COM), CaOx dyhydrate (COD) and CaOx trihydrate (COT) as displayed in Fig. 1.1. Among them, COM is the most thermodynamically stable and most frequently found stone in the kidneys [1].

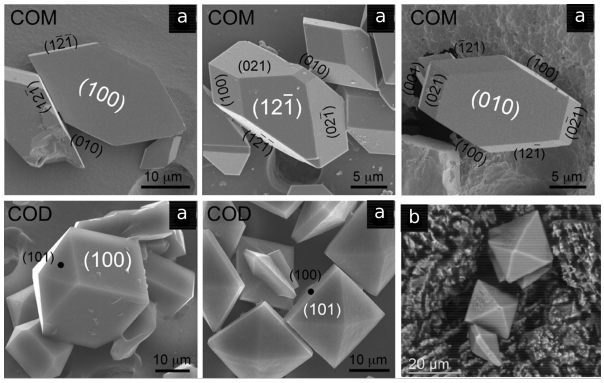

Figure 1.1: SEM of COM and COD. [37] (a) and COD on the surface of marble [33] (b)

The stone formation is not caused by a single reason but caused by several reasons such as [5, 20, 30, 39]:

- High supersaturation and concentrations of stone-forming substances like calcium, phosphorus, oxalate and low urine volume.
- Low concentrations of inhibitors like citrate, phospahtes and magnesium.
- High concentrations of promoters like uric acid.

1.3. Research objectives

The goal of this research is to study the influence of mass transport of calcium (Ca) and oxalate (Ox) ions from bulk solution to the crystal surface at different constant flow rates on the growth rate of the CaOx stone. ANSYS/Fluent CFD was used to determine the supersaturation profile in the microchannel for different constant flow rates and Ca and Ox inlet concentrations, which is needed for the CaOx growth rate data analysis. A Polydimethylsiloxane (PDMS) microfluidic device was used to mimic the collecting duct in kidney. The crystal growth rate were measured with a aid of an optical microscope which provided a continuous observation of growth during the entire experiment. Then, the CaOx stone growth rate is determined by using a Kassemi combined transport-kinetics model in which both mass transfer of ions to the crystal surface and reaction on the growing crystal surface are taken into account. The understanding of the CaOx stone mechanism is essential to provide valuable information in preventing the disease to occur.

2

Theoretical Background

2.1. Supersaturation

It is well known from the experimental data that supersaturation is the driving force for the crystallization process. Supersaturation is defined as the chemical potential difference between the mother phase and the daughter phase at the same temperature and pressure [35, 41]. The spontaneous crystallization occurs when the chemical potential of the mother phase is larger than that of daughter phase. In other words, the solution precipitates when the solute concentration is larger than the equilibrium concentration.

$$\Delta\mu = \mu_{mother} - \mu_{crystal} = \mu_{mother} - \mu_{mother}^{eq} \tag{2.1}$$

where μ_{mother} is the chemical potential of solute in the mother phase being crystallized and μ_{mother}^{eq} is the chemical potential of solute at equilibrium in the mother phase. In a solution, the chemical potential of solute is described by:

$$\mu_B = \mu_B^*(T,P) + \mathrm{R}T \ln x_B \gamma_B \tag{2.2}$$

where $\mu_B^*(T,P)$ is the hypothetical standard state, x_B is the solute mole fraction and γ is the solute activity coefficient.

Combination of Eqs. 2.1 and 2.2 gives:

$$\Delta\mu = \mathrm{R}T \ln \frac{\gamma c}{\gamma_{eq} c_{eq}} \tag{2.3}$$

where c is the solute concentration being crystallized and c_{eq} is the solute concentration at equilibrium.

In general, the extent of supersaturation or relative supersaturation can be defined as [18]:

$$\sigma = \frac{\Delta\mu}{\mathrm{R}T} = \ln\frac{\gamma c}{\gamma_{eq} c_{eq}} \tag{2.4}$$

If the activity coefficient γ is not influenced by the concentration, then in a given concentration range there is γ=γ_{eq}, the eqn2.4 becomes:

$$\sigma = \ln\frac{c}{c_{eq}} \approx \frac{c - c_{eq}}{c_{eq}} \tag{2.5}$$

The term $c - c_{eq}$ represent the concentration driving force Δc. For practical use, the supersaturation ratio is expressed by [26]:

$$S = \frac{c}{c_{eq}} \tag{2.6}$$

and relative supersaturation is expressed by [27]:

$$\sigma = \frac{\Delta c}{c_{eq}} = S - 1 \tag{2.7}$$

When two crystallizing components are involved such as Ca and Ox ions, the concentrations in eqn. 2.6 are replaced by the concentration products of the two components [10, 11, 26]:

$$S = \left(\frac{C_{Ca^{2+}} C_{Ox^{2-}}}{C_{Ca^{2+},eq} C_{Ox^{2-},eq}}\right)^{1/2} = \left(\frac{C_{Ca^{2+}} C_{Ox^{2-}}}{K_{sp}}\right)^{1/2} \tag{2.8}$$

where K_{sp} is the solubility product. Strictly speaking, the Ca and Ox concentrations in eqn.2.8 should be corrected with the consideration of an activity coefficient activities γ due to the fact that interaction between Ca-Ca ions or Ox-Ox ions is different than that between Ca and Ox ions. The Eqn. 2.8 becomes:

$$S = \left(\frac{C_{Ca^{2+}} C_{Ox^{2-}} \gamma^2}{K_{sp}}\right)^{1/2} \tag{2.9}$$

Thus, in order to determine an accurate supersaturation value it is needed to find ion activity by calculating the activity coefficient.The activity coefficient can be calculated by several activity models. In this study, the Davies equation has been chosen to calculate the activity coefficient due to the fact that it is capable of calculating activity coefficient over a moderate range of dilute solutions [28]:

$$-\log\gamma_i = AZ_i^2\left(\frac{\sqrt{I}}{1+\sqrt{I}}\right) - 0.3I \tag{2.10}$$

where γ_i is the ion activity for species i, Z_i is the charge of the i^{th} ion in the electrolyte and A is the Debye-Huckel constant, which has a value of 0.509 at 25°C for water [28].

I is the ionic strength of the solution which can be calculated by the following relation:

$$I = \frac{1}{2}\sum C_i Z_i^2 \tag{2.11}$$

where C_i and Z_i are the concentration and the charge of the i^{th} ion in the electrolyte.

In this study, the equations above were solved by Herman's Solchem program code using MATLAB.

In the crystallization process, three regions of saturation can be recognized which are represented in Fig. 2.1.

1. Unsaturated region at Point a: crystals of all sizes will be dissolved when added to the solution
2. Metastable region at Point c: Point c is between Point b and d. At point b, the solution is saturated and no more crystals will be dissolved. In the metastable region, there is no crystal nucleation but the existing crystal can still grow.
3. Unstable region: the supersaturation is high enough to make spontaneous nucleation occur. The crystals can also grow.

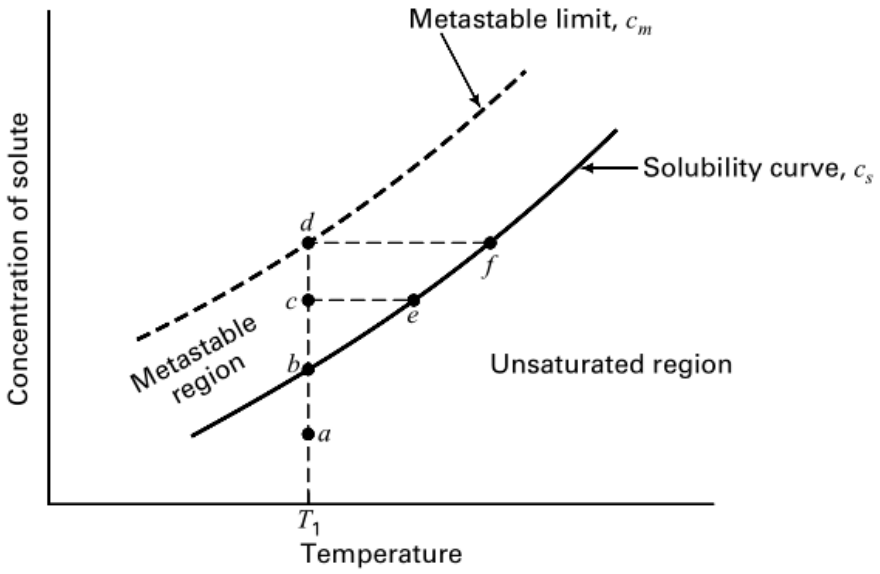

Figure 2.1: Representative solubility–supersolubility diagram [16]

2.2. Nucleation

Crystallization is a solid-liquid phase transformation process in which crystalline particles are formed from a homogeneous solution. One of the important concepts in phase transformation is the nucleation. Nucleation can be separated into two parts: homogeneous and heterogeneous. Homogeneous nucleation is unaided by any surface or defects. Heterogeneous is aided by container wall, grain boundaries, impurities and defects and etc.

2.2.1. Homogeneous nucleation

Nucleation is the first stage of the formation of new phases. The nucleus will be formed when it has reached the critical radius r^*. Critical radius is determined by free energy change (ΔG_f) due to formation of a solid particle of radius r in liquid as an energy barrier to the nucleation process. To be simplified, it is assumed a spherical solid nucleus in a liquid (Fig. 2.2) has the same density as that of liquid, thus no volume change on transformation.

$$\Delta G_f^{homo} = \frac{4}{3}\pi r^3 (G_s - G_L) + 4\pi r^2 \gamma_I \tag{2.12}$$

In Eqn. 2.12 [38]the first part is the volume free energy, ΔG_v which is negative in supersaturation solution. The second part is the surface free energy, $\Delta G_{surface}$ which results from the formation of solid-liquid phase boundary during the phase transformation [42]. G_s represents free energy per unit volume of solid and G_L represents free energy per unit volume of liquid. γ_I is energy per unit area of the solid-liquid interface. These energy as function of radius is shown in Fig. 2.3.

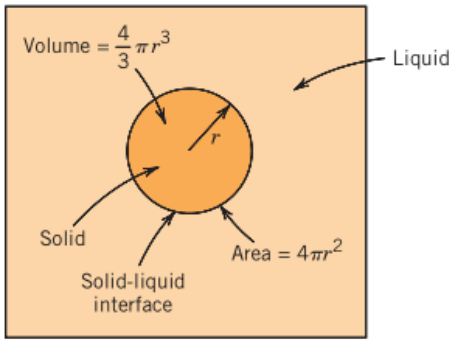

Figure 2.2: The nucleation of a spherical solid particle in a liquid. [42].

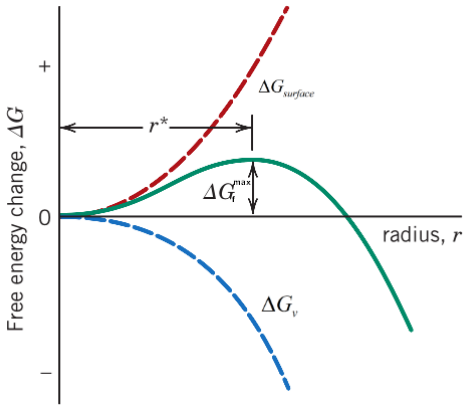

Figure 2.3: Free energy as a function of radius.

Critical radius is located at which ΔG_f^{homo} is maximum. If the particle radius is less than r^*, the growth is thermodynamically not favorable, causing the particle to shrink and redissolve. If the particle reaches a size corresponding to r^*, the particle will continue to grow.

Applying the condition for maximum ΔG_f^{homo}:

$$\left.\frac{\partial \Delta G_f^{homo}}{\partial r}\right|_{r=r^*} = 0 \tag{2.13}$$

which leads to:

$$r^* = \frac{-2\gamma_I}{\Delta G_v} \tag{2.14}$$

Substitution of Eqn.2.14 into Eqn.2.12 gives:

$$\Delta G_f^{homo} = \frac{16\pi {\gamma_I}^3}{3(\Delta G_v)^2} \tag{2.15}$$

2.2.2. Heterogeneous nucleation

In case of heterogeneous nucleation, nucleation is more likely to take place at the container wall rather than inside the liquid. To be simplified, it is assumed a spherical solid nucleus is formed from a liquid phase at on a plat surface. The interfacial energies are presented in Fig. 2.4 and the interfacial energy balance in the plane of the flat surface is expressed by [42]:

$$\gamma_{IL} = \gamma_{SI} + \gamma_{SL}\cos\theta \tag{2.16}$$

where γ_{IL}, γ_{SI} and γ_{SL} are surface-liquid, solid-surface and solid-liquid interfacial energies respectively. The volume of a solid particle, V_s is expressed by:

$$V_s = \frac{4}{3}\pi r^3 S(\theta) \tag{2.17}$$

where,

$$S(\theta) = \frac{2 - 3\cos\theta + \cos^3\theta}{4} \tag{2.18}$$

The solid-liquid and solid-surface interfacial area are expressed by:

$$A_{SL} = 4\pi r^2\left(\frac{1-\cos\theta}{2}\right) \tag{2.19}$$

and

$$A_{SI} = \pi r^2(1-\cos^2\theta) \tag{2.20}$$

Combination of equations above leads to the result:

$$\Delta G_f^{het} = V_s\Delta G_v + A_{SL}\gamma_{SL} + A_{SI}\gamma_{SI} - A_{SI}\gamma_{IL} \tag{2.21}$$

The last term of ΔG_f^{het} can be considered as additional driving force. Applying the condition for maximum ΔG_f^{het}:

$$\left.\frac{\partial \Delta G_f^{het}}{\partial r}\right|_{r=r_{het}^*} = 0 \tag{2.22}$$

which leads to:

$$r_{het}^{*} = \frac{-2\gamma_{SI}}{\Delta G_v} \tag{2.23}$$

Substitution of Eqn. 2.23 into Eqn. 2.24 gives:

$$\Delta G_f^{het} = \frac{16\pi {\gamma_{SL}}^3}{3(\Delta G_v)^2} S(\theta) \tag{2.24}$$

where $S(\theta)$ has a numerical value between 0 and 1, indicating the shape of the solid spherical cap. Therefore, it is capable of explaning why heterogeneous nucleation is favoured over homogeneous nucleation.

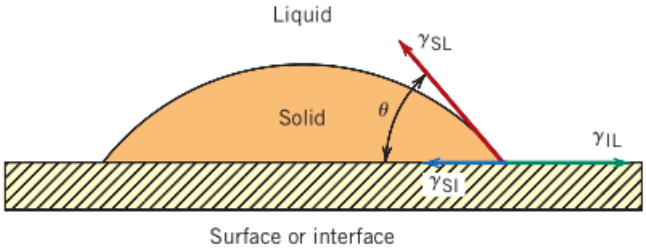

Figure 2.4: Heterogenous nucleation of a solid from a liquid [42].

2.3. The Growth Rate

Once a nidus has formed, the nucleus will continue to grow into a macroscopic crystal. This second step of the crystallization process is defined as crystal growth. Crystal growth is controlled by a number of factors. These include the 3D crystal structure and crystal defects which influence the intermolecular interactions between the crystal surface. In addition, the presence of impurity, supersaturation and temperature also play important roles in crystal growth [27, 32].

The growth process can be separated into the following stages [3, 17]:

1. Diffusion of substances from the mother bulk phase to the crystal surface.
2. Surface diffusion of substances from a given site on the crystal surface to energetically favorable sites.
3. Incorporation of the substances into the crystal lattice.

2.3.1. The Kossel and Stranski Theory

The concept of nonequivalent of sites on the crystal surface was first realized by Stranski. In this model, the growth unit was simplified as a cubic block. The three types of attachment sites for growth units to grow at the crystal surface are displayed in Fig. 2.5.

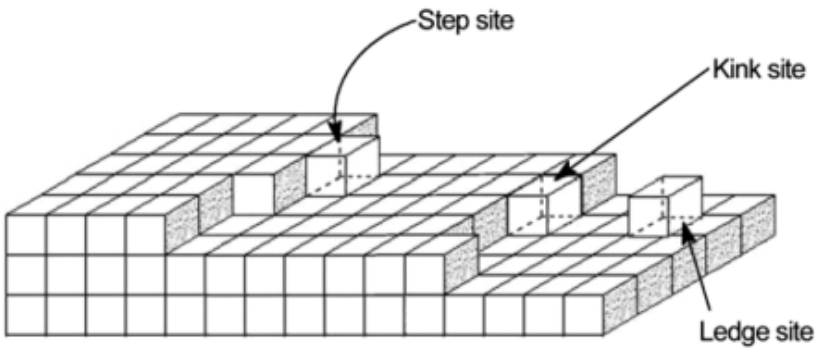

Figure 2.5: Illustration of growth process on two-dimensional surface [12].

The growth unit will diffuse to kink site that is most energetically stable, i.e. where the greatest energy is released. At kink site, the growth unit gets the maximum contact with the crystal surface, hence maximum binding energy between them and least probability of dissolution. Thus, the growth units are incorporated into the kink sites one after another repeatedly until rows are formed [3]. A new layer is started by forming a 2D nucleus at flat surface that is not so stable. This step is energetically unfavourable and would occur at supersaturation 25% to 50% whereas according to experiments many crystals require less than 1% [13]. This was mainly due to crystal defects which will be discussed in the following section.

2.3.2. The Burton Cabrera and Frank Theory

In the previous Kossel-Stranski model, the crystal is assumed to be ideal without any lattice defects. A more promising crystal growth model was proposed by Frank and his coworkers who assumed that the real crystals are imperfect and steps are originated during crystal growth on dislocations [4]. Dislocations are defeats or irregularity within the crystal lattice structure when the lattice atoms move from regular ideal position as shown in Fig. 2.6.

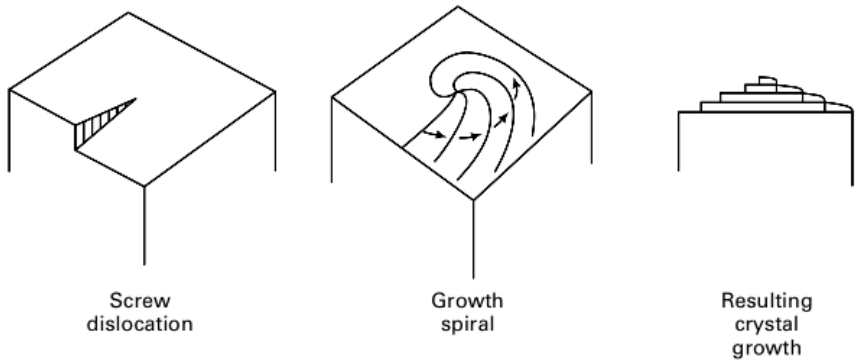

Figure 2.6: Screw-dislocation mechanism of crystal growth [16].

Dislocations act as fault site which minimize the energy barrier, providing easier incorporation of new grow units and a new way to form surface uninterrupted while avoiding the high energy demanded 2D nucleation [4, 6, 41]. The surface then continue to grow in a spiral manner around the dislocation center. This model is able to explain why crystals grow at very low supersaturation.

Many studies showed the parabolic rate law for electrolytes of different valence types both at low and high supersaturation. Meyer and Smith studied crystal growth of CaOx in a stable supersturated solution and found the rate law takes the form [22]:

$$-\frac{dc}{dt} = kN^2 \tag{2.25}$$

where -dc/dt is the rate of disappearance from solution of component c, k is the rate constant and N is the difference between component c activity at saturation and any time t. Marc observed the same dependence for potassium sulphate in the experiment in which the growth rate is proportional to $(c - c_s)^2$ [31]. Nielsen proposed a crystal growth mechanism based on the BCF model that is capable of explaining the parabolic nature of the surface reaction. As explained by Nielsen [25], the growth rate of salts is governed by both kinetic and thermodynamic factors. One of the (S-1) second order term indicating the flux rate of incorporation of ions into the crystal surface per kink while the other (S-1) factor comes from the density of kinks on the crystal surface.

For many sparingly soluble inorganic salts M_aX_b, the deposition rate of ions onto the crystal surface is expressed by Eqn. 2.26 [13].

$$\frac{dn}{dt} = -k_r'' s K_{sp}^{p/v} \sigma^p \tag{2.26}$$

where n is the moles of salts precipitated, k_r'' is the surface reaction rate constant, p is the effective order of the reaction, s is a function of the surface area of the crystals and v is the sum of a and b and σ is the relative supersaturation.

3

Supersaturation simulation using CFD tools

This chapter will deal with the outcomes of simulation results using CFD under different conditions. The modeling equations are solved numerically to study the supersaturation profile in microchannel with different Ca and Ox inlet concentrations and inlet flow rates. A 3D model of the microchannel used in the experiment will be structured in this simulation.

3.1. Introduction

In this study, the three-dimensional simulations have been performed with the industrial ANSYS/Fluent CFD (Computational Fluid Dynamics) code. Fluent is one of the widely used CFD software package with great success in all fields of engineering applications and scientific research. CFD is a powerful tool to solve complex partial differential equations governing conversational mass and energy law by a set of algebraic equations. Fluent software package used in this study uses the finite volume method (FVM) to find the numerical solutions of partial differential equations. In the CFD technique, the flow domain is divided into a number of finite-sized sub-domains (control volume). Each domain is represented by a finite number of grid points. The governing differential equations are discretized and solved in integral form. Then, the initial conditions and boundary conditions are used to solve these equations. These equations are solved iteratively until the solution reaches the desired accuracy. Additionally, FVM carries the physical meaning of conservation with itself. As differential equation is an equation which is valid at a point, it states the principle of conservation mathematically at a point. By integrating the differential equation over the domain it will imply that the same conservation principle over the domain are satisfied in an integral form.

3.2. Governing Equations

In this section the computational fluid dynamics modeling equations for the behavior of fluids and chemical species in microfluidic channel are described.

3.2.1. Continuity Equation

The equation for conservation of mass, or continuity equation is as follows:

$$\frac{\partial \rho}{\partial t} + \nabla \cdot (\rho \cdot \vec{v}) = 0 \tag{3.1}$$

where ρ is the density of the fluid and $\vec{v}$ is the velocity field vector of the fluid. The first term on the left-hand side of Eqn. 3.1 is the rate of change of mass in a small element of fluid and the second on the left-hand side is the net rate of flow of mass across a small element surface.

3.2.2. Momentum Conservation Equation

Momentum conservation equation (equation of motion/ Navier-Stokes equation) involving a Newtonian fluid with the assumptions of impressibility and constant viscosity is written as:

$$\rho\left(\frac{\partial \vec{v}}{\partial t} + (\vec{v} \cdot \nabla)\,\vec{v}\right) = -\nabla P + \mu \nabla^2 \vec{v} + \rho \vec{g} + \vec{F} \tag{3.2}$$

where P is the pressure, μ is the dynamic viscosity of the liquid, $\rho\vec{g}$ and $\vec{F}$ are the gravitational body force and external body forces. The acceleration on the left-hand side of the equation has two components: the local acceleration and the convective acceleration. The local acceleration term is also known as unsteady term which represents how the velocity of the element fluid changes with respect to time. The convective acceleration term is also known as steady term which represents how the velocity changes as a particle fluid moves from one location to another location. In a 3-dimensional Cartesian coordinate system (x,y,z), the ∇ (Nabla operator) is defined as $\left(\left(\frac{\partial}{\partial x}\right),\left(\frac{\partial}{\partial y}\right),\left(\frac{\partial}{\partial z}\right)\right)$ and the ∇^2 (Laplace operator) is defined as $\left(\left(\frac{\partial^2}{\partial x^2}\right),\left(\frac{\partial^2}{\partial y^2}\right),\left(\frac{\partial^2}{\partial z^2}\right)\right)$.

3.2.3. Species transport Equation

Transport of Ca and Ox ions through the microchannel is described by the species transport equation by setting up a mole balance over a small element volume. The differential equation that governs the transport of species is expressed by the convection-diffusion equation for the two ionic species as:

$$\frac{\partial c_i}{\partial t} + D_{i,m} \nabla^2 c_i - \vec{v} \cdot \nabla c_i = 0 \tag{3.3}$$

for i= Ca, Ox

where $D_{i,m}$ is the molecular diffusivity in m^2/s and c_i is the concentration of ionic species i. The first term in the equation describes the transient transport of the mass, the second term describes the

diffusion flux due to concentration gradients using Fick's law and the final term describes the convection of mass caused by the flow.

3.3. Simulation Setup

This section will deal with the computational model that has been built in this study. The modeling equations are solved numerically to study the supersaturation at different Ca and Ox inlet concentrations and different flow rates.

3.3.1. Geometry and Mesh

A 3D model of the microchannel used in the experiment was structured in simulation. The microchannel has a length of 1300 µm, a depth of 45 µm and a width of 295 µm. The microchannel can be separated into two parts. The upper part has a width of 145 µm and the bottom part has a width of 150 µm. Geometrical details are given in Fig. 3.1.

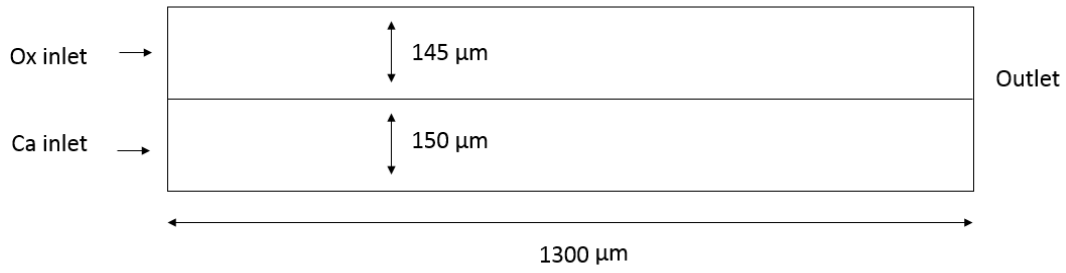

Figure 3.1: Schematic view of the microchannel geometry used for this study

A 3D geometry of the microchannel was construced in ANSYS workbench and is shown in Fig. 3.2 Quadrilateral mesh was used for meshing the geometry shown in Fig. 3.3 It was meshed into 110760 elements.

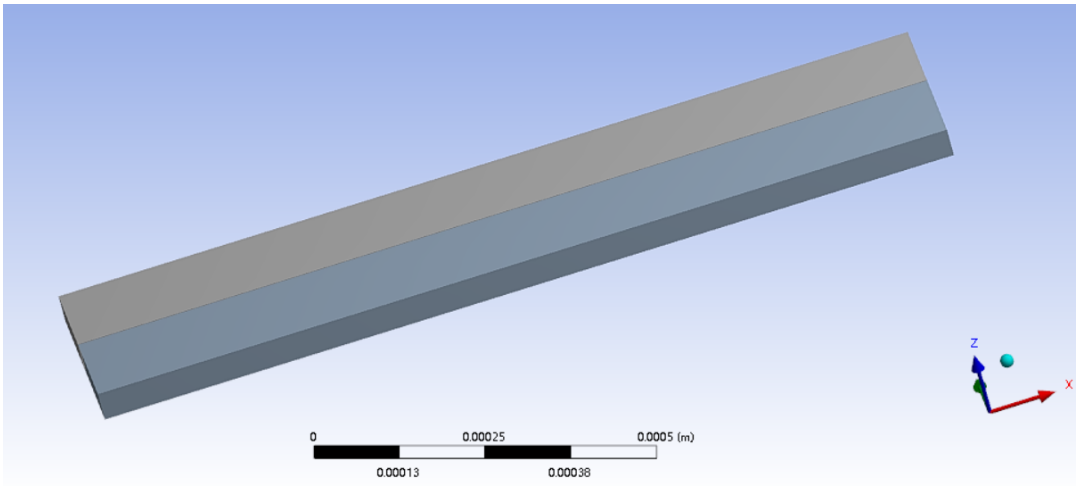

Figure 3.2: Geometry of the microchannel in ANSYS workbench

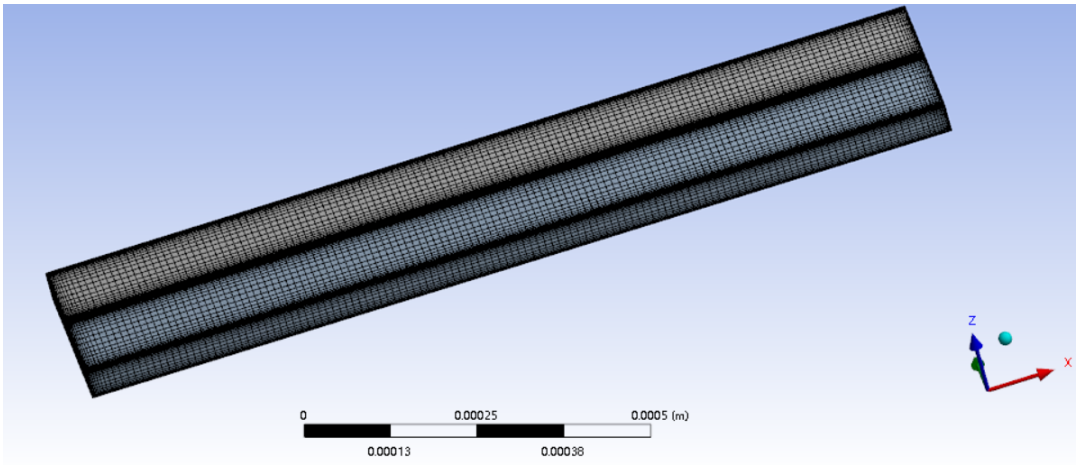

Figure 3.3: Quadrilateral mesh of the microchannel geometry

The physical dimensions and operating conditions are listed in Table. 3.1

Parameter	Unit	Range or Value
Length X Width X Depth of the microchannel	m X m X m	1.3×10^{-3} X 295×10^{-6} X 45×10^{-6}
Ox inlet microchannel width	m	145×10^{-6}
Ca inlet microchannel width	m	150×10^{-6}
Inlet flow rate of solution	m^3/s	2.0×10^{-10} to 1.3×10^{-9}
Inlet concentration of Ox	mol/L	0.0039, 0.0004
Inlet concentration of Ca	mol/L	0.0039, 0.012
Diffusion coeffcient of Ox and Ca	m^2/s	1×10^{-8} [2]
Activity coefficient γ	dimensionless	0.7577, 0.5959

Table 3.1: Physical dimensions and operating conditions used in simulation

3.3.2. Boundary conditions and Method of solution

To solve the equations in the simulation, boundary conditions for the computational domain were implemented. The pressure outlet boundary condition was set to the microchannel outlet. A no-slip boundary condition was imposed to the interface between the solid wall and liquid. For the ionic species transport process, the walls were set to no flux. Flow rate and concentration of the solution were specified at the inlet of the microchannel. The laminar model was implemented based on Reynolds number (Re) which determines the nature of fluid flow. Re is the ratio of the inertial effects to the viscous effects of the fluid written as:

$$\mathrm{Re} = \frac{\rho \mathrm{v} D_h}{\mu} \tag{3.4}$$

where v is the average velocity of the fluid, ρ is the density of the fluid and D_h is the characteristic length dimension. In general, when Re for a liquid traveling through a pipe or vessel below 2100 the flow is laminar. In laminar flow, the fluid particles move in a same straight line without any lateral mixing. The flow in microchannel is generally laminar since the dimensions of microfluidic system is small. In this

work, the Re is 6 for the largest velocity used in the microfluidic experiments. Thus, this study will deal with fluid flow at low Re that falls within the laminar flow region.

For the velocity and pressure fields, the pressure-based solver was used to numerically solve the continuity and momentum equations. For the pressure-velocity coupling method, a coupled scheme was used. All governing equations were solved using the finite volume approach.

3.4. Results and Discussion

The microchannel has two separate streams where the Ox ions enter through the top inlet and the Ca ions enter through the bottom inlet. As the two streams enter and meet in the microchannel, the two species will only mix through diffusion by moving in a direction transverse to the flow direction. Convective mixing of fluid will not occur since the fluid in the microchannel flows in a laminar pattern. In reality, simultaneously to the diffusion of the species, the precipitation reaction between the two species will also happen. But in this study, the reaction is not considered. The supersaturation was calculated based on Eqn. 2.9 The simulation results of supersaturation in Fig. 3.4 were carried out for bulk Ca concentration 0.0039 M, bulk Ox concentration 0.0039 M and inlet flow rate of 1.3 $\times$ 10^{-9} m^3/s.

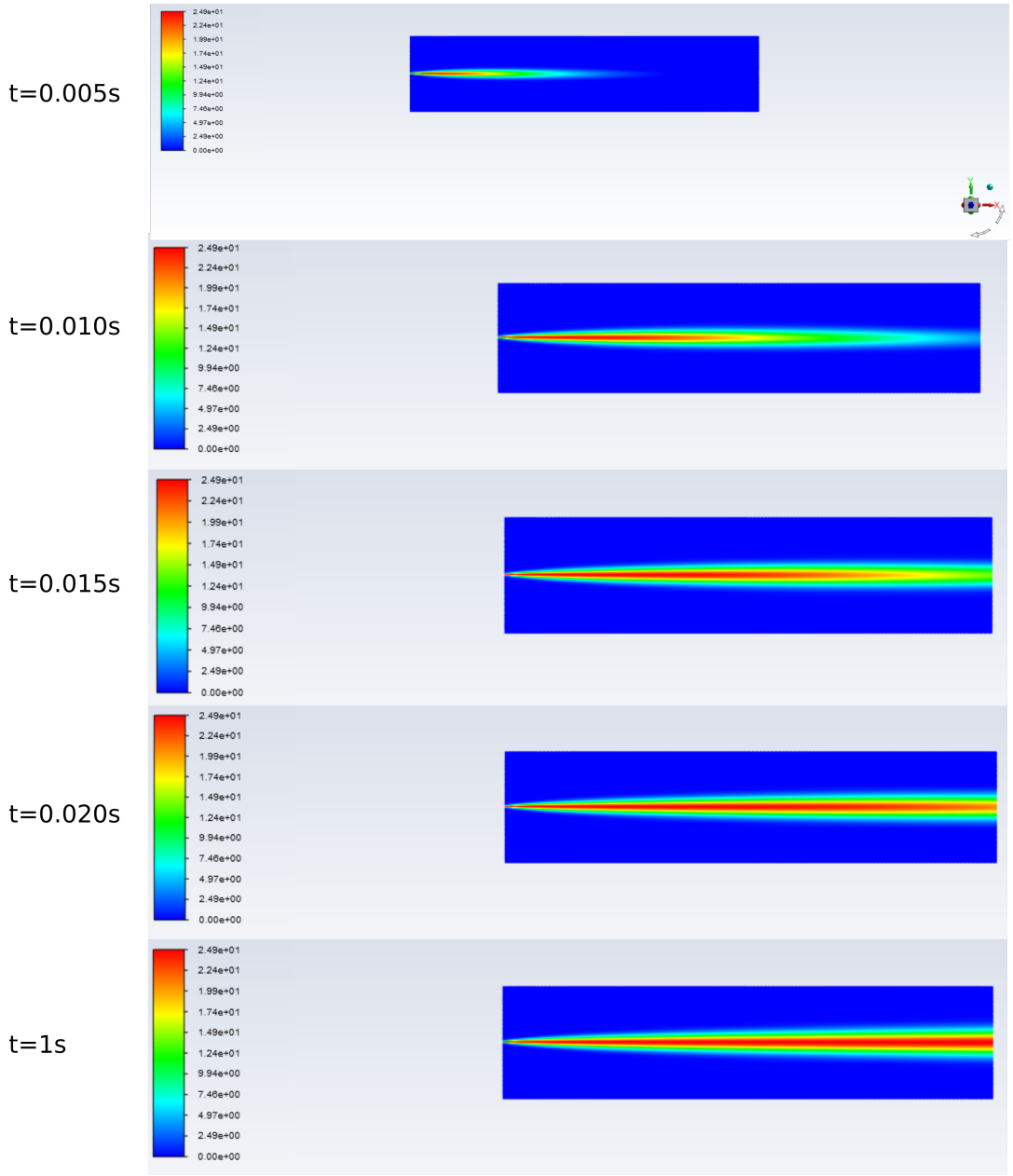

Figure 3.4: The supersaturation profile at different time steps with with Ca and Ox inlet concentration=0.0039 M, mean velocity=0.10 m/s (inlet flow rate=1.3$\times$ 10^{-9} m^3/s) at z=8.5 μm.

The simulation results of supersaturation in Fig. 3.5 were carried out for bulk Ca concentration 0.012 M, bulk Ox concentration 0.0004 M and inlet flow rate of 10 $\times$ 10^{-10} m^3/s. The contours of supersaturation profiles were all plotted at z=8.5 μm since the microscope was focused on the microchannel wall with depth of field of 8.5 μm. Fig. 3.4 and Fig. 3.5 show that the supersaturation reached the steady state condition within 1s. In addition to that, all the supersaturation profiles under other conditions in this simulation also reached the steady state condition within 1s. As the transient time is much shorter than the experimental operating time, for the following analysis of simulation results will be presented based on the steady state condition.

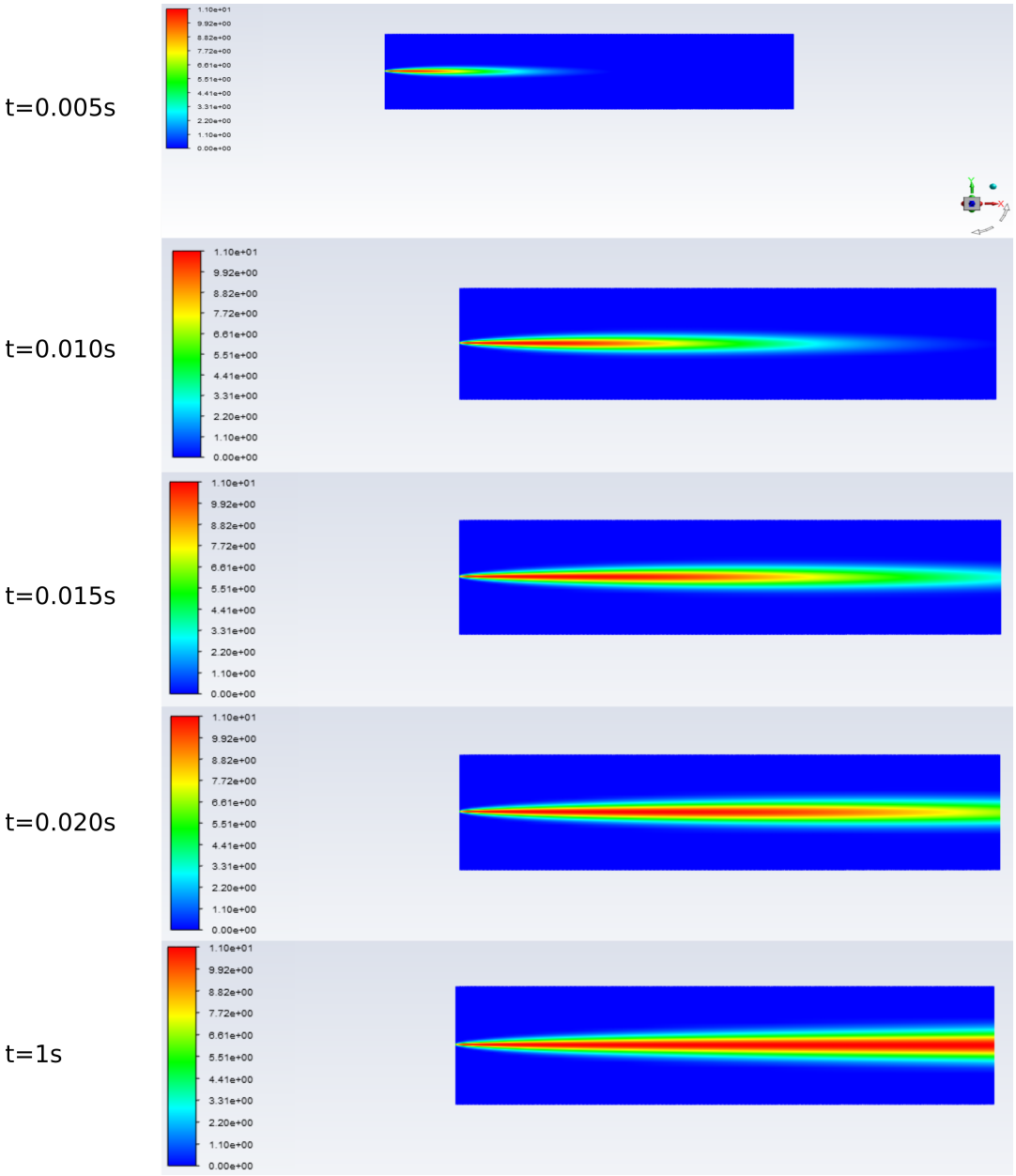

Figure 3.5: The supersaturation profile at different time steps with with Ca inlet concentration=0.012 M and Ox inlet concentration=0.0004 M, mean velocity=0.075 m/s (inlet flow rate= 10 $\times 10^{-10}$ m^3/s) at z=8.5 μm.

3.4.1. Mixing of ionic species

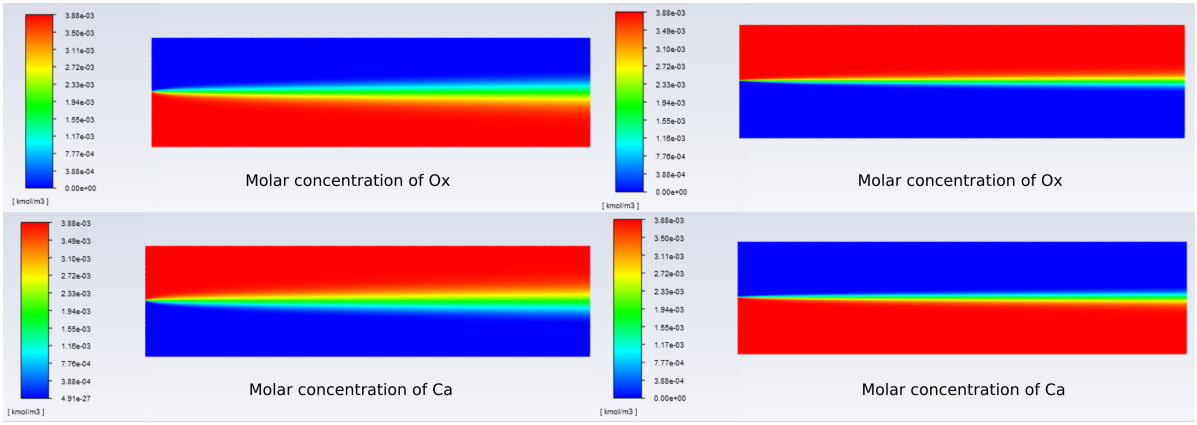

Figure 3.6: Concentration profiles for different constant total flow rates with Ca and Ox inlet concentration=0.0039 M at z=8.5 μm. (a) mean velocity=0.02 m/s (2 cm/s), flow rate= 2.7 $\times$ 10^{-10} m^3/s. (b) mean velocity=0.10 m/s (10 cm/s), inlet flow rate= 1.3 $\times$ 10^{-9} m^3/s.

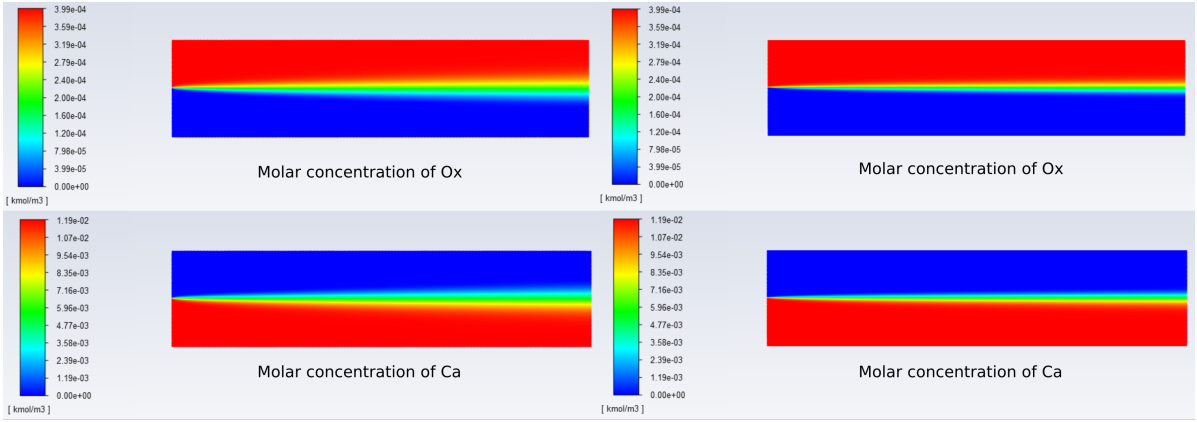

Figure 3.7: Concentration profiles for different constant total flow rates with Ca inlet concentration=0.012 M and Ox inlet concentration=0.0004 M at z=8.5 μm. (a) mean velocity=0.015 m/s (1.5 cm/s), flow rate= 2 $\times$ 10^{-10} m^3/s. (b) mean velocity=0.075 m/s (7.5 cm/s), inlet flow rate= 10 $\times$ 10^{-10} m^3/s.

In both above figures, the bottom Ca part of the microchannel is located at y= -150 µm and the upper Ox part of the channel is located at y= 145 µm. The position at x= 0 µm and y= 0 µm is where two streams separated before they meet in the microchannel. The simulation result as shown in both figures finds that Ox stays mostly confined to the upper part of the microchannel while the Ca stays mostly confined to the bottom part of the mirochannel. Thus, the fluid flows over the microchannel in a side-by-side arrangement.

The concentration profile has a narrow shape at the entrance of the microchannel but a broader shape at the end of the microchannel. This is because that the ionic species can diffuse further away from the centre of the microchannel in the direction reverse to flow as going further down the microchannel. Moreover, the concentration profiles shown in Fig. 3.6 and Fig. 3.7 in the microchannel have different constant flow rates, which determine the convection time scale for a fixed geometry. The convection

time scale refers to the time taken for convection from the inlet to the outlet of the channel. When the convection time increases, the ionic species have more time to diffuse across the central microchannel. When the convection time decreases, the ionic species will tend to remain in the original stream. As Fig. 3.6 (a) and (b) or Fig. 3.7 (a) and (b) compares, when the convection time number becomes smaller, the diffusion becomes less important.

3.4.2. supersaturation profile

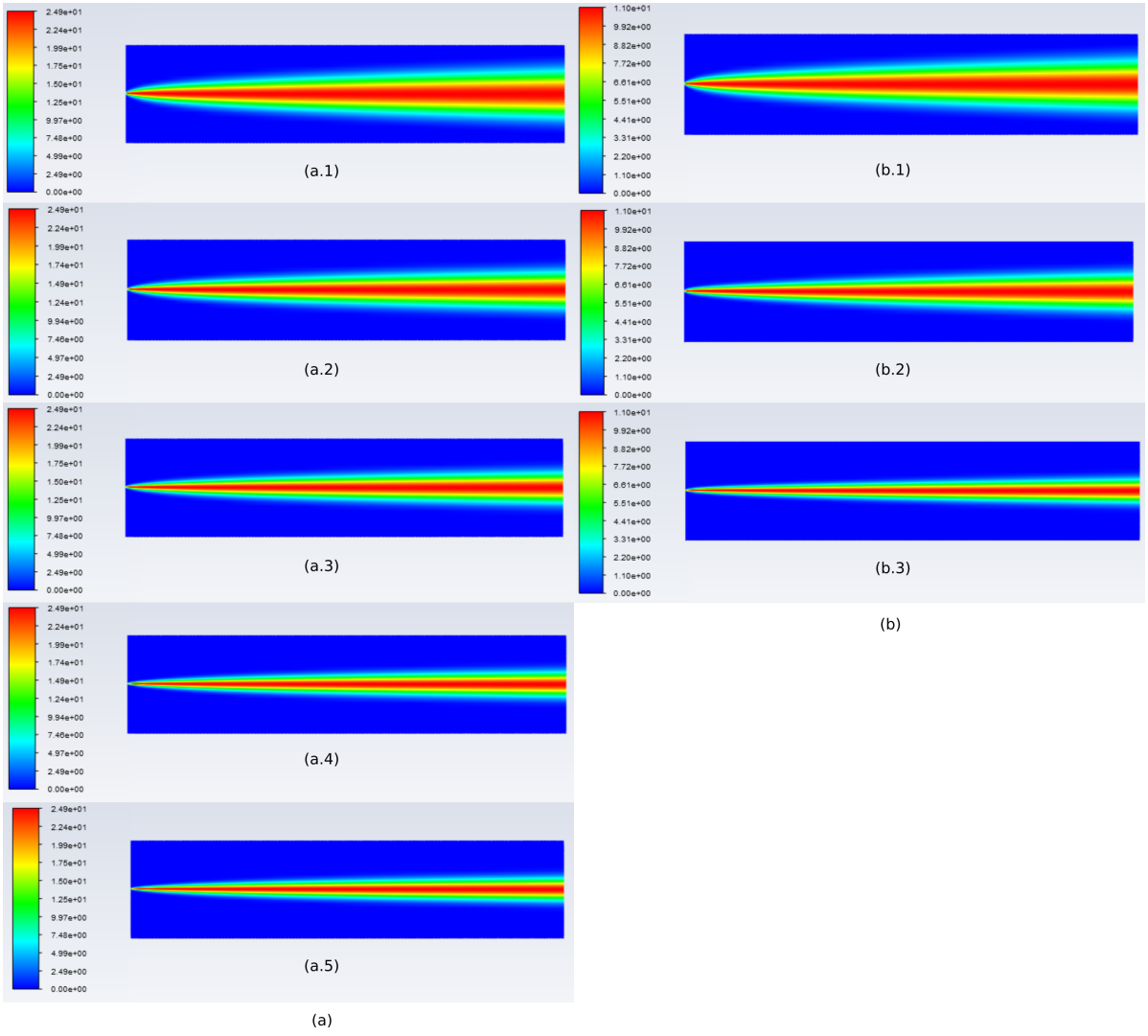

Figure 3.8: Supersaturation profiles for different constant total flow rates at z=8.5 μm with (a) Ca inlet concentration=0.0039 M and Ox inlet concentration=0.0039 M (a.1) flow rate= 2.7× 10^{-10}, mean velocity=0.020 m/s (2.0 cm/s) (a.2) flow rate= 5.0× 10^{-10}, mean velocity=0.038 m/s (3.8 cm/s) (a.3) flow rate= 7.0× 10^{-10}, mean velocity=0.070 m/s (7.0 cm/s) (a.4) flow rate= 1.1× 10^{-9}, mean velocity=0.084 m/s (8.4 cm/s) (a.5) flow rate= 1.3× 10^{-9}, mean velocity=0.10 m/s (10 cm/s) (b) Ca inlet concentration=0.012 M and Ox inlet concentration=0.0004 M (b.1) flow rate= 2.0× 10^{-10}, mean velocity=0.015 m/s (1.5 cm/s) (b.2) flow rate= 4.6× 10^{-10}, mean velocity=0.035 m/s (3.5 cm/s) (b.3) flow rate= 10× 10^{-10}, mean velocity=0.075 m/s (7.5 cm/s)

The supersaturation profiles in the microchannel with different Ca and Ox inlet concentrations and different constant flow rates in Fig. 3.8 were evaluated according to the Eqn. 2.9.

Besides the contour plots, the variation in supersaturation with y-coordinate for different x width position of the microchannel is shown in Fig. 3.9. For other flow rates, the supersaturation figures can be found in Appendix. A. In all the curves in Fig. 3.9, the maximum supersaturation is reached near the centre of the microchannel at position y ≈-1 µm. The interface is not found at y= 0 µm because the width of the upper part of the microchannel is smaller than that of the bottom part of the microchannel. Therefore, it results in a higher velocity in the upper part, moving the interface little bit downward. As same as in the concentration profiles, as going further down the microchannel, the supersaturation curve gets broader due to the diffusion.

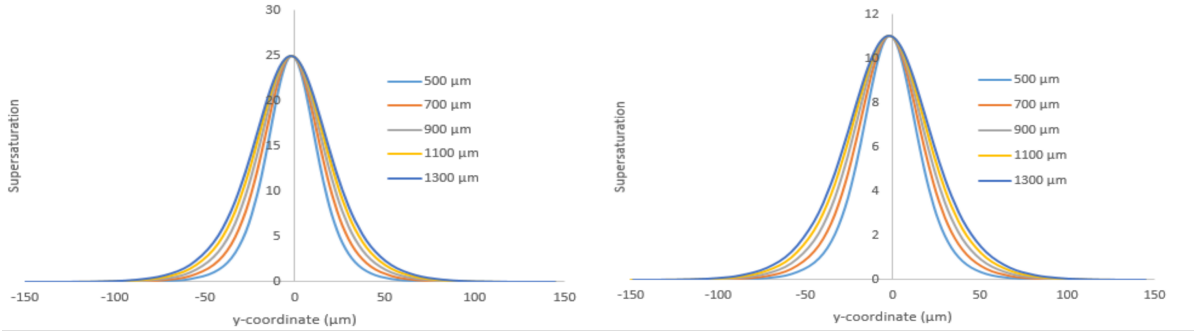

Figure 3.9: The variation in supersaturation with y-coordinate for different x width position of the microchannel at z=8.5 μm with (a) Ca inlet concentration=0.0039 M and Ox inlet concentration=0.0039 M, flow rate= 1.3× 10^{-9}, mean velocity=0.10 m/s (10 cm/s) (b) Ca inlet concentration=0.012 M and Ox inlet concentration=0.0004 M, flow rate= 10× 10^{-10}, mean velocity=0.075 m/s (7.5 cm/s).

In Table. 3.2 and Table. 3.3 the supersaturation slope values at position 6 µm away from the interface in y-direction for different Ca and Ox inlet concentrations and different constant flow rates are given.

Flow rate (m^3/s)	Mean velocity (m/s)	Mean velocity (cm/s)	ΔS / Δy aty_{int} ± Δy and x= 500 µm (1/µm)	ΔS / Δy at y_{int} ± Δy and x= 700 µm (1/µm)	ΔS / Δy at y_{int} ± Δy and x= 900 µm (1/µm)	ΔS / Δy at y_{int} ± Δy and x= 1100 µm (1/µm)	ΔS / Δy at y_{int} ± Δy and x= 1300 µm (1/µm)
2.7×10^{-10}	0.02	2	0.02	0.01	0.007	0.005	0.005
5.0×10^{-10}	0.038	3.8	0.06	0.03	0.02	0.01	0.01
7.0×10^{-10}	0.07	7	0.09	0.06	0.04	0.03	0.02
1.1×10^{-9}	0.084	8.4	0.2	0.1	0.07	0.05	0.04
1.3×10^{-9}	0.1	10	0.2	0.1	0.1	0.07	0.06

Table 3.2: The supersaturation slope at various x-positions for different constant total flow rates at z=8.5 μm with Ca inlet concentration=0.0039 M, Ox inlet concentration=0.0039 M and Δy= 6 µm, y_{int}=interface position at y-coordinate.

Flow rate (m^3/s)	Mean velocity (m/s)	Mean velocity (cm/s)	ΔS / Δy at y_{int} ± Δy and x= 500 µm (1/µm)	ΔS / Δy at y_{int} ± Δy and x= 700 µm (1/µm)	ΔS / Δy y_{int} ± Δy and x= 900 µm (1/µm)	ΔS / Δy at y_{int} ± Δy and x= 1100 µm (1/µm)	ΔS / Δy at y_{int} ± Δy and x= 1300 µm (1/µm)
2.0×10^{-10}	0.015	1.5	0.05	0.04	0.03	0.03	0.02
4.6×10^{-10}	0.035	3.5	0.08	0.07	0.05	0.05	0.04
10×10^{-10}	0.075	7.5	0.1	0.1	0.09	0.09	0.08

Table 3.3: The supersaturation slope at various x-positions for different constant total flow rates at z=8.5 μm with Ca inlet concentration=0.012 M, Ox inlet concentration=0.0004 M and Δy= 6 µm, y_{int}=interface position at y-coordinate.

The tables above show that the supersaturation values at x= 500 µm and 6 µm away from the interface in y-direction deviate from the maximum value. Both tables indicate that the slopes of the supersaturation curves decrease as the x-coordinate increases. Thus, for the microfluidic CaOx growth rate experiments the crystal particles in the region $y_{interface}$ ± Δy, x >500 µm were analysed for the

size measurement.

It should be noted that there are two reasons that cause the supersaturation values in Fig. 3.8 to deviate from the true value. One reason is because the precipitation reaction is not incorporated in the model, indicating the supersaturation values in the microchannel were overestimated. Another reason is that in all the cases it was assumed that the activity coefficients were constant in the simulation. However, the activity coefficient is a function of ionic concentration. The activity coefficient increases as the concentration of ions decreases. Thus, the activity coefficients were underestimated at position away from the centre of the microchannel and also the supersaturation values.

4

Calcium Oxalate Crystal Growth

This chapter will deal with the CaOx crystal growth under different conditions with varying supersaturation, velocity and Ca and Ox inlet solution concentrations on the centre line. The materials and method regarding microfluidic experiment will be presented. A Kassemi transport- kinetics combined model for the growth of CaOx crystal will be given. In the results section, both experimental and modelling results will be discussed.

4.1. Materials and Method

4.1.1. Materials and Equipment

The growth rate of CaOx was examined inside the microchannel with an aid of an optical microscope. The materials used to prepare the PDMS microfluidic chip are summarized in Table. 4.1. All chemicals used were of analytical grade and were used as received without any further purification.

Substance	Chemical Formula	CAS Number	Vendor
Sodium Oxalate	$Na_2C_2O_4$	62-76-0	Sigma-Aldrich
Calcium Chloride	$CaCl_2$	10043-52-4	Sigma-Aldrich
Ultrapure Water	H_2O		Elga
Trichlorosilane	$NCF_3(CF_2)_5CH_2CH_2SiCl_3$	78560-45-9	Sigma-Aldrich
Polydimethylsiloxane	$(C_2H_6OSi)n$		The DOW Chemical Company
2-propanol	C_3H_8O	67-63-0	Sigma-Aldrich
Osteopontin human	-	SPR3131	Sigma-Aldrich

Table 4.1: List of chemicals used in the experiments

A list of equipment used in the experiments is shown in Table. 4.2.

Equipment	Equipment Name	Brand
Scale	Mettler PM2000	Mettler Toledo
Ultrasonic bath	Branson 2510 Ultrasonic Cleaner	Branson
Oven		Binder
Centrifuge	Universal 320 R	Hettich Zentrifugen
Dessicator		Kartell
Spincoater		Polos
Microscope	Zeiss Axiovert-200M	Zeiss
	Nikon Eclipse Ti	Nikon
Pressure pump	MFCS - EZ	Fluigent

Table 4.2: List of equipment used in the experiments

4.1.2. Microfluidic Chip Manufacturing

In a plastic tube, the PDMS was mixed in a 1:7 ratio of curing agent and PDMS monomers. The mixture was stirred with spatula until it filled up with many air bubbles and became cloudy. In order to remove the bubble, the mixture was kept in centrifuge for 15 minutes at 7400 rpm. Before pouring PDMS into the silicone wafer, the silicone wafer (Fig. 4.1) needs to be coated with a thin layer of trichlorosilane to make the peeling process easier. This was done by placing a small drop of trichlorosilane and silicone wafer upside down into the desiccator for 2 hours at pressure 100 mbar. The trichlorosilane coated silicone wafer can be used 4 times.

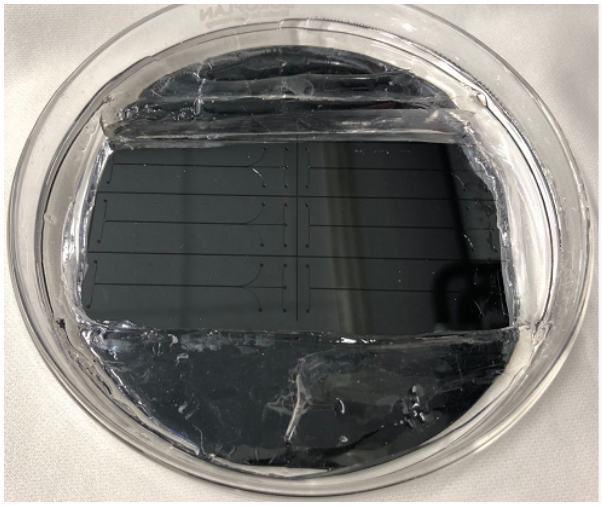

Figure 4.1: silicone wafer

The PDMS was then degassed in the desiccator by vacuum at 500, 300, 200, 100 and 30 mbar sequentially to prevent sudden rush of air knocking over the wafer. A few small bubbles on the PDMS surface are acceptable since they do not effect the device's performance. After degassing for 1 hour vacuum was released slowly and the degassed PDMS was then placed inside an oven overnight at

65°C, allowing the PDMS to harden. Holes were punched at the inlets and outlet of the PDMS chip. The solid PDMS with desired microchannel pattern can be used to bond a glass slide.

Both the glass slide and PDMS chip were cleaned with methanol to prevent dirt from clogging the channels. A small drop of PDMS mixture in a 1:10 ratio of curing agent and PDMS monomers was poured onto the glass slide. Then, they were spin-coated, leaving a thin film layer of PDMS mixture on the glass slide. After that the glass slide was place in an oven at 90 °C for about 15 minutes. The stickiness of PDMS thin film layer was repeatedly checked to ensure if it is cured enough to bond to the PDMS chip. Once the glass slide and PDMS chip were bonded, they were placed into the oven overnight at 65°C to be completely cured. The PDMS chip was punched with three holes, two for inlets and one for outlet. The open end of the PDMS chip was then sealed by applying the UV curing agent (UV curing adhesive glue) and placing it under ultraviolet light for about 5 minutes. After that, the PDMS chip (Fig.4.4)was tested for the leakage.

4.1.3. Solution Preparation

The quantity of calcium chloride and sodium oxalate used in the microfluidic experiments is shown in Tabel.4.3.These chemicals were dissolved in ultra pure water by ultrasonic homogenization. For the Osteopontin (OPN) inhibitor experiments the calcium chloride and sodium oxalate were kept at 0.012 M and 0.0004 M respectively. OPN stock solution was prepared by dissolving 50 µg of OPN in 6.25 mL of ultra pure water, giving a concentration of 8 µg/mL. Then, the OPN stock solution was added into the sodium oxalate stock solution to a required concentration. The prepared OPN stock solution was stored in the fridge at -20°C. The list of used molar ratio between OPN and Ca for the OPN inhibitor experiments is shown in Table. 4.4.

Molar ratio Ca:Ox	**Calcium chloride (mol/L)**	**Calcium chloride (g/100mL)**	**Sodium oxalate (mol/L)**	**Sodium oxalate (g/100mL)**
1:1	0.00389	0.00389	0.0432	0.0521
30:1	0.012	0.133	0.0004	0.00536

Table 4.3: Quantity of chemical needed for preparing solutions for microfluidic experiments.

Molar ratio OPN: Ca	**OPN mass concentration in stock solution where both sodium oxalate and OPN present (µg/mL)**
2×10^{-6}	1.44
5×10^{-6}	3.60
7×10^{-6}	5.04

Table 4.4: Molar ratio OPN:Ca for OPN inhibitor experiments.

4.1.4. Experimental Setup

For the CaOx growth rate experiment, both calcium chloride and sodium oxalate aqueous solution were prepared. The two 1.5 mL reservoirs connected with pressure pump (Fig.4.6) were filled with solutions. The capillary tubing (Warner Insturments, 0.28 mm inner diameter) was used to connect reservoirs and PDMS microchip. The pressure was controlled via AIO software provided by Fluigent. The flow rate was calculated by weighing the amount of water pushed through the microchannel at different pressure. The setup of the experiment is given in Fig. 4.2 and Appendix. B.1.

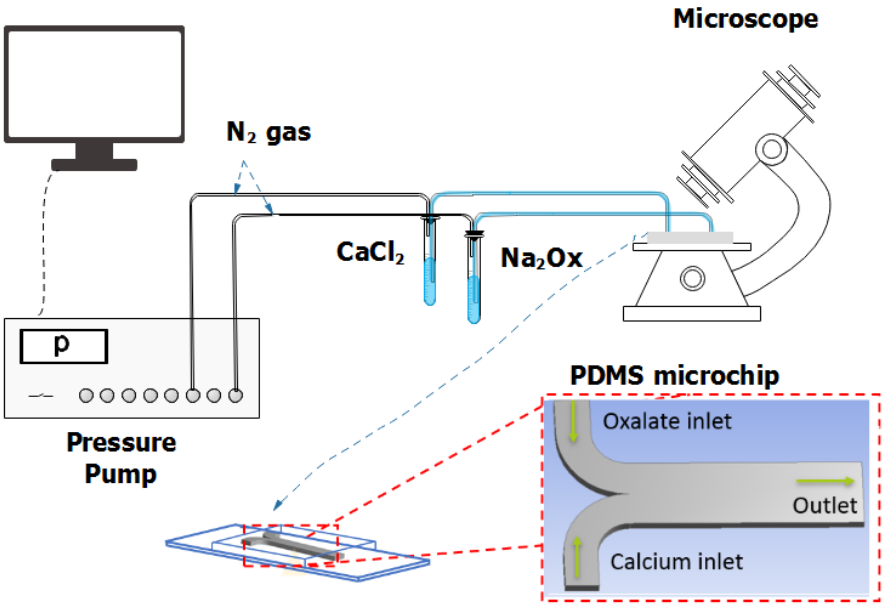

Figure 4.2: Schematic setup of the CaOx crystal growth microfluidic experiment.

Air bubbles (Fig. 4.3) will block or obstruct flow and are sometimes very difficult to remove. In order to prevent air bubbles getting into the microchannel during the experiment, an experimental protocol was developed with following steps:

1. The microchannel was filled with de-ionized water
2. The reservoirs were filled up with solution by injecting the solution through the tubes into them.
3. The inlet tubes were filled with solutions ensuring no air is in the tip of the tubes
4. The inlet tubes were inserted into the microchannel while kept the fluids inside the inlet tubes flowing at 5 mbar.
5. The pressure was set up at the desired value.

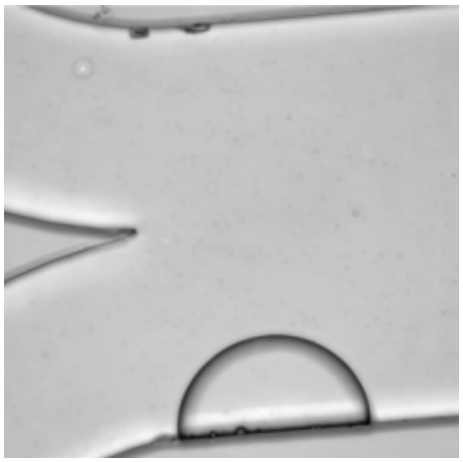

Figure 4.3: Air bubble inside microchannel

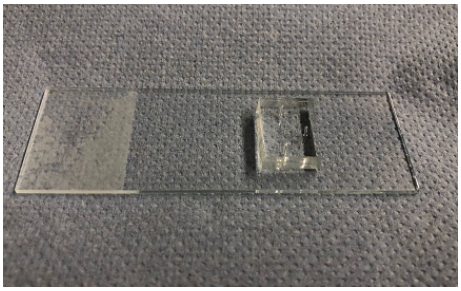

Figure 4.4: PDMS microchip

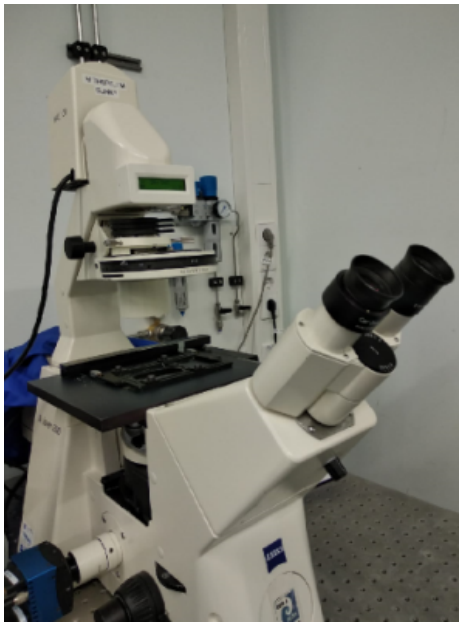

Figure 4.5: Zeiss Axiovert-200M microscope

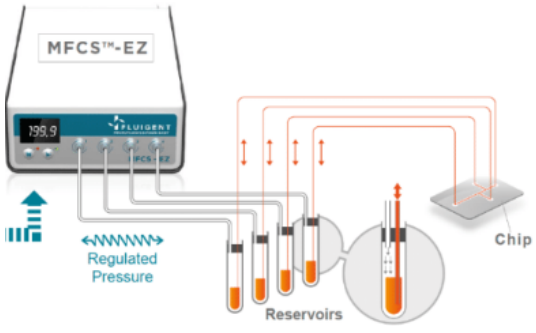

Figure 4.6: MFCS - EZ Fluigent pressure pump[9]

4.1.5. Mathematical Model of Crystal Growth

Symbol	Definition	Symbol	Definition
C	dimensionless concentration at the crystal surface	$\dot{r}$	growth rate (cm/s)
C^*	concentration at the surface (mol/L)	Re	flow Reynolds number
C_∞	dimensionless bulk liquid concentration	S_{inf}	bulk solution supersaturation
C_∞^*	bulk liquid concentration	Sh	Sherwood number
Da	Damkohlernumber	Sc	solution Schmidt number
D_{im}	molecular diffusion coefficient (cm^2/s)	U	relative crystal-fluid velocity
γ	activity coefficient	V_M	molar volume (M_w/ρ)
K_m	film mass transfer coefficient (cm/s)	M_w	molecular weight
K_r	surface reaction rate constant (cm/s)(L/mol)	ρ	crystal density (g/L)
K_{sp}	equilibrium solubility product $(mol/L)^2$	v_m	kinematic viscosity (cm^2/s)

Table 4.5: Nomenclature

A spherical CaOx crystal particle with radius r is considered, which grows in water at uniform bulk Ca and Ox concentrations. It is postulated that the growth process is controlled by a balance between the transport of ions from the bulk to the surface and the kinetics of surface reaction of ions that grow on the crystal surface. The growth rate of the crystal can be written as follows [13, 19, 24, 36]:

$$\dot{r} = \frac{dr}{dt} = K_r V_m K_{sp}\left[\left(\frac{C_{Ca}^* C_{Ox}^* \gamma^2}{K_{sp}}\right)^{1/2} - 1\right]^2 \tag{4.1}$$

In this formula, C_{Ca}^* and C_{Ox}^* are the concentration of Ca and Ox ions in the liquid at the crystal surface. K_r [8, 22] is the surface reaction rate constant for CaOx crystal formation, V_m is the molar volume of CaOx, K_{sp} is the equilibrium solubility product and γ is a divalent activity coefficient. The formula shows that in order to obtain the crystal growth rate, the surface concentration of Ca and Ox ions need to be determined. This can be achieved by mass balance, balancing consumption of Ca and Ox ions by the crystallization reaction at the crystal surface and the supply rates of these ions from the bulk solution to the crystal surface. Thus, the unknown surface concentrations of each ion can be solved by the mass balances shown as below:

$$K_m\left(C_{Ox}^* - C_{\infty,Ox}^*\right) = -K_r K_{sp}\left[\left(\frac{C_{Ca}^* C_{Ox}^* \gamma^2}{K_{sp}}\right)^{1/2} - 1\right]^2 \tag{4.2}$$

and

$$K_m\left(C_{Ca}^* - C_{\infty,Ca}^*\right) = -K_r K_{sp}\left[\left(\frac{C_{Ca}^* C_{Ox}^* \gamma^2}{K_{sp}}\right)^{1/2} - 1\right]^2 \tag{4.3}$$

In these equations, the diffusion coefficients for Ca and Ox ions is assumed to be equal. Thus, K_m represents the film mass transfer parameter, which is same for both Ca and Ox ions. The equations can be transformed into simple form by defining dimensionless concentrations, C_{Ca} and C_{Ox}, and a dimensionless, Damkohler number, Da. Da represents the ratio between the surface reaction rate and the mass transfer rate [14].

$$C_{Ca} = \frac{C_{Ca}^*}{K_{sp}^{1/2}} \tag{4.4}$$

,

$$C_{Ox} = \frac{C_{Ox}^*}{K_{sp}^{1/2}} \tag{4.5}$$

and

$$Da = \frac{K_r {K_{sp}}^{1/2}}{K_m} \tag{4.6}$$

The Eqn. 4.2 can be changed to:

$$\left(C_{Ox} - C_{\infty,Ox}\right) = -Da\left[\left(C_{Ca}C_{Ox}\gamma^2\right)^{1/2} - 1\right]^2 \tag{4.7}$$

The film mass transfer parameter K_m can be written by incorporating the Sherwood number (Sh), as

$$K_m = \frac{ShD_{im}}{d} \tag{4.8}$$

The Sherwood number is used in forced convection mass transfer correlations. The Sherwood number can be estimated from an empirical Frossling equation [34, 36] for flow around a spherical particle.

$$Sh = 2 + 0.6Re^{1/2}Sc^{1/3} \tag{4.9}$$

In the equation above, Re and Sc are flow Reynolds number and Schmidt numbers, respectively, defined as followed equations.

$$\mathrm{Re} = \frac{Ud}{v_m} \tag{4.10}$$

and

$$Sc = \frac{v_m}{D_{im}} \tag{4.11}$$

Where U is relative velocity between the crystal and fluid, d is crystal diameter, v_m is the kinematic viscosity of solution, D_{im} is molecular diffusion coefficient.

With all the equations above, the growth rate of crystal can be calculated under different conditions. The nonlinear mass balance equations for both species can be solved numerically by Newton-Raphson method using Matlab. The list of physiochemical parameters in the analysis is presented in Fig. 4.6.

Parameters	Value
V_m	0.066 (L/mol) [8]
K_{sp}	3.479×10^{-9} $(mol/L)^2$ [23]
K_r	22 (L/mol)(cm/s) [8]
ρ	2200 (g/L) [8]
D_{im}	10^{-4} (cm^2/s) [2]
v_m	8.17 × 10^{-3} (cm^2/s) [2]

Table 4.6: Physiochemical parameters.

4.2. Results and Discussion

The flow rates at pressure 20 mbar to 60 mbar were calculated by weighing the amount of water pushed through the microchannel three times. The velocities presented in Table. 4.7 were calculated by taking the flow rates over the cross section area of the microchannel.

Pressure (mbar)	Velocity 1 (cm/s)	Velocity 2 (cm/s)	Velocity 3 (cm/s)	Mean velocity (cm/s)	Standard deviation
0	0	0	0	0	0
20	1.3	0.9	1.2	1.1	0.14
30	2.2	1.9	2.0	2.0	0.13
40	3.1	2.7	2.8	2.9	0.13
50	3.9	3.9	3.6	3.8	0.15
60	4.8	4.7	4.2	4.6	0.21
70	5.5	5.3	4.9	5.3	0.21
110	8.7	8.6	7.8	8.4	0.35
130	10.3	10.2	9.2	10	0.42

Table 4.7: Velocities at different pressures.

The velocity at 70 mbar to 130 mbar were estimated by means of linear extrapolation. The results are shown in Fig. 4.7

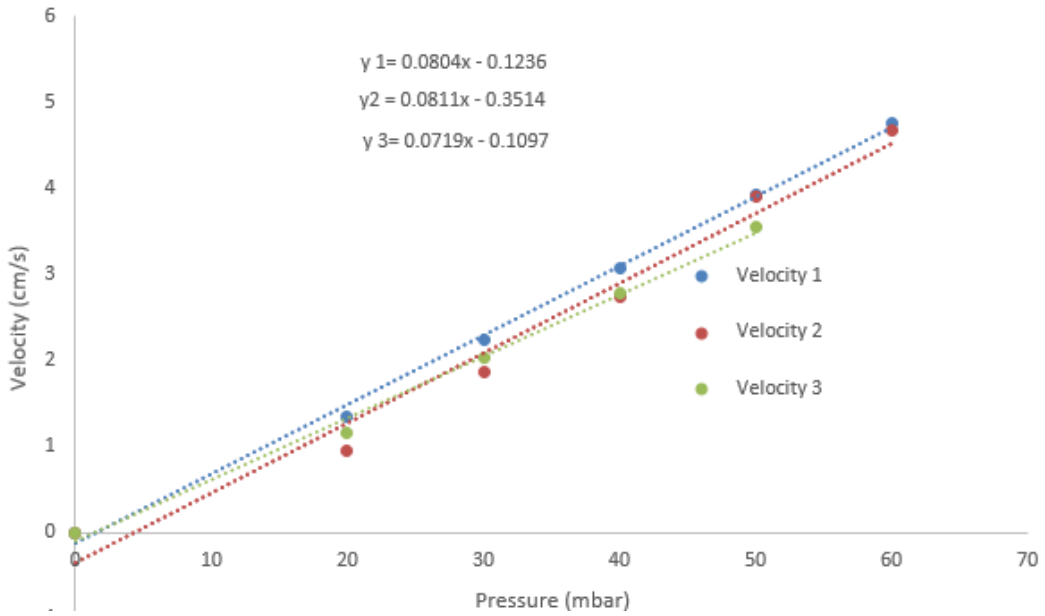

Figure 4.7: Velocities at different pressures.

4.2.1. Crystal growth of equal Ca and Ox concentrations

In this study, the CaOx growth was studied under Zeiss Axiovert-200M series microscope (Fig. 4.5) fitted with a high magnification camera (Mikrotron MC3011). 5x magnification was used with the focus on the PDMS microchannel wall where the crystals are stationary (fixed) for imaging CaOx crystal size. When crystals were visible to naked eyes, images were taken and then analyzed by a scientific image processing software ImageJ. In Fig. 4.8 the CaOx crystallization process inside the microchannel is illustrated.

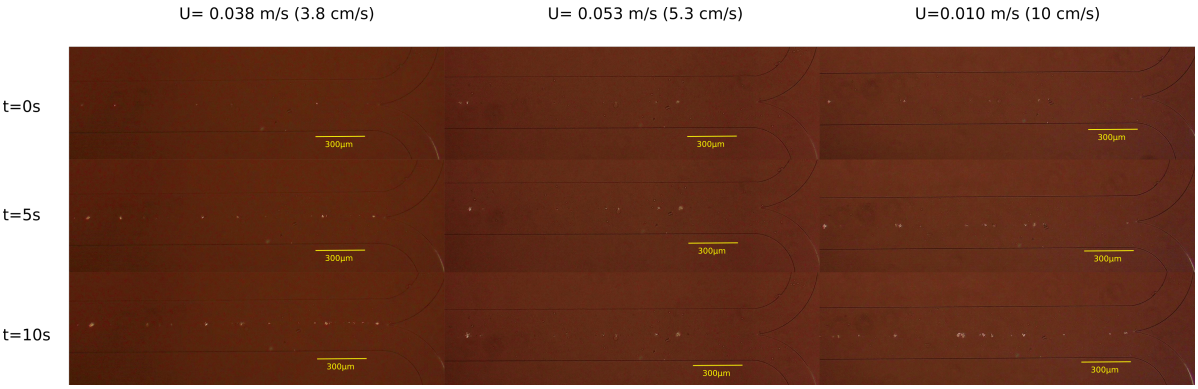

Figure 4.8: CaOx crystallization process inside the microchannel under 5x magnification under the Zeiss microscope

The radius of CaOx particle was calculated based on the particle area by assuming CaOx particle is to be spherical. The radius started to be analyzed at the time when there a number of CaOx particles occurred inside the microchannel. Growth rate of CaOx crystals for different relative velocities with equal solution concentration is presented in Table. 4.8. The mean radius of CaOx versus time for relative velocity U=0.02 m/s (2.0 cm/s) is shown in Fig. 4.9 and that for the other pressures is shown in the appendix. C.

Pressure (mbar)	Velocity (cm/s)	Velocity (m/s)	Growth rate (cm/min)	Growth rate (m/s)	95% Confidence interval (cm/min)	95% Confidence interval (m/s)
30	2	0.02	2.84×10^{-4}	4.73×10^{-8}	2.34×10^{-4}, 3.36×10^{-4}	3.90×10^{-8}, 5.60×10^{-8}
50	3.8	0.038	2.81×10^{-4}	4.68×10^{-8}	2.32×10^{-4}, 3.31×10^{-4}	3.89×10^{-8}, 5.52×10^{-8}
70	5.3	0.053	2.65×10^{-4}	4.42×10^{-8}	2.06×10^{-4}, 3.24×10^{-4}	3.43×10^{-8}, 5.40×10^{-8}
110	8.4	0.084	2.52×10^{-4}	4.20×10^{-8}	2.10×10^{-4}, 2.94×10^{-4}	3.50×10^{-8}, 4.90×10^{-8}
130	10	0.1	2.84×10^{-4}	4.73×10^{-8}	2.30×10^{-4}, 3.39×10^{-4}	3.83×10^{-8}, 5.65×10^{-8}

Table 4.8: Growth rate in different relative velocities with equal solution inlet concentrations $C^*_{\infty,ca}$=$C^*_{\infty,ox}$=0.0039 (mol/L)

In Fig. 4.9, the linear changes in mean CaOx radius over time was extrapolated to estimated the growth rate when the relative velocity U is 3.8 cm/s. The fluctuations in data might be caused by the formation of nucleation and agglomeration and they did not affect the overall trend drawn from analyzing the rest of the data. The results in Table. 4.8 showed that the effect of relative velocity on the CaOx growth rate is quite limited.

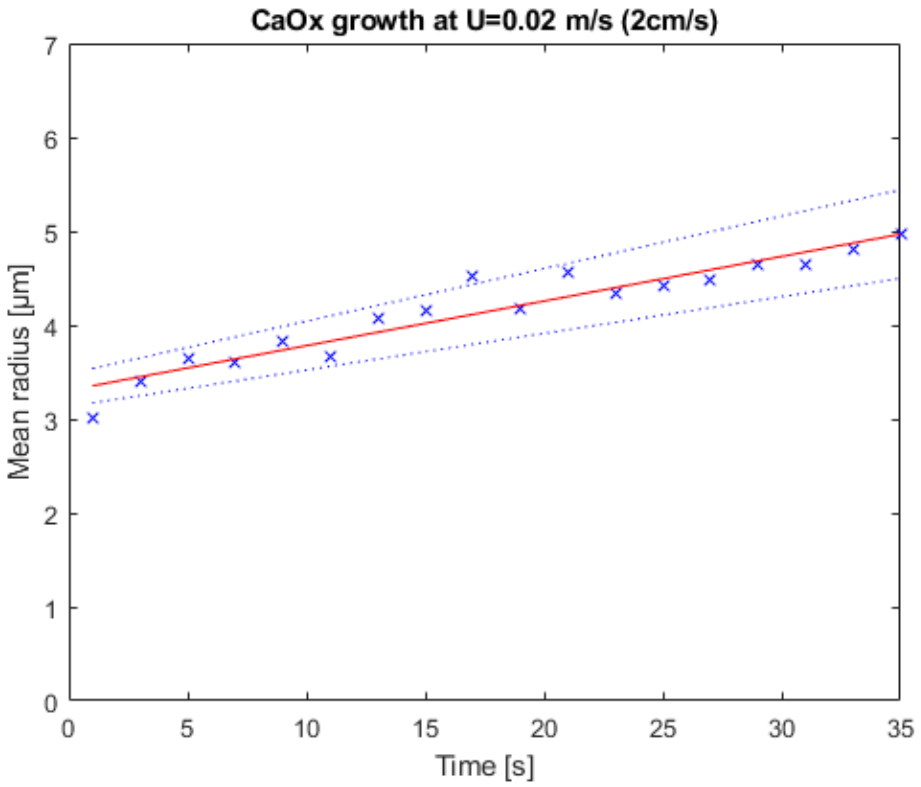

Figure 4.9: CaOx mean radius vs time for relative velocity U=0.020 m/s (2.0 cm/s) with equal inlet solution concentration $C^*_{\infty,ca}$=$C^*_{\infty,ox}$=0.0039 (mol/L)

A comparison between experimental data and modelling results for the CaOx growth rate in different relative velocities is presented in Fig. 4.10. The physiochemical parameters used in this model are presented in Table. 4.6. In which, the uninhibited and unpromoted reaction rate constant is based on the measurements done by Meyer and Smith [22]. It shows a relative good qualitative match between the experimental data and modelling growth rate prediction. Quantitatively, both results show the magnitude of growth rate is in an order of 10^{-8} m/s. However, the experimental obtained growth rate is higher than the modeling obtained growth rate. A possible reason is that the surface reaction constant is higher than expected.

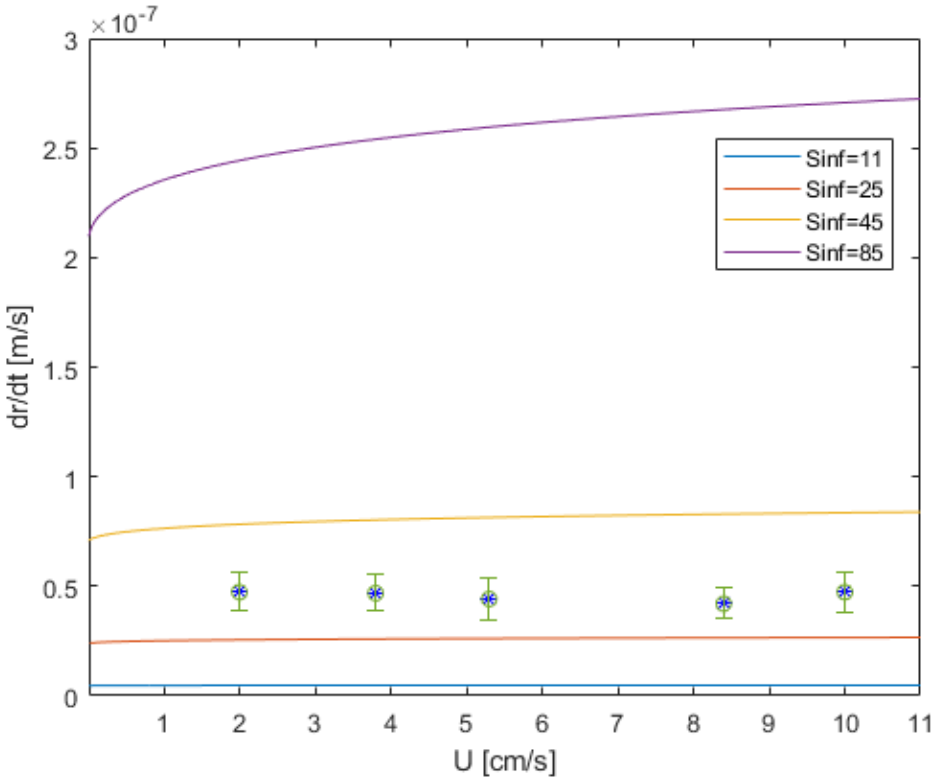

Figure 4.10: Effect of relative velocity U on the CaOx growth rate for different solution supersaturation based on equal Ca and Ox solution concentration .

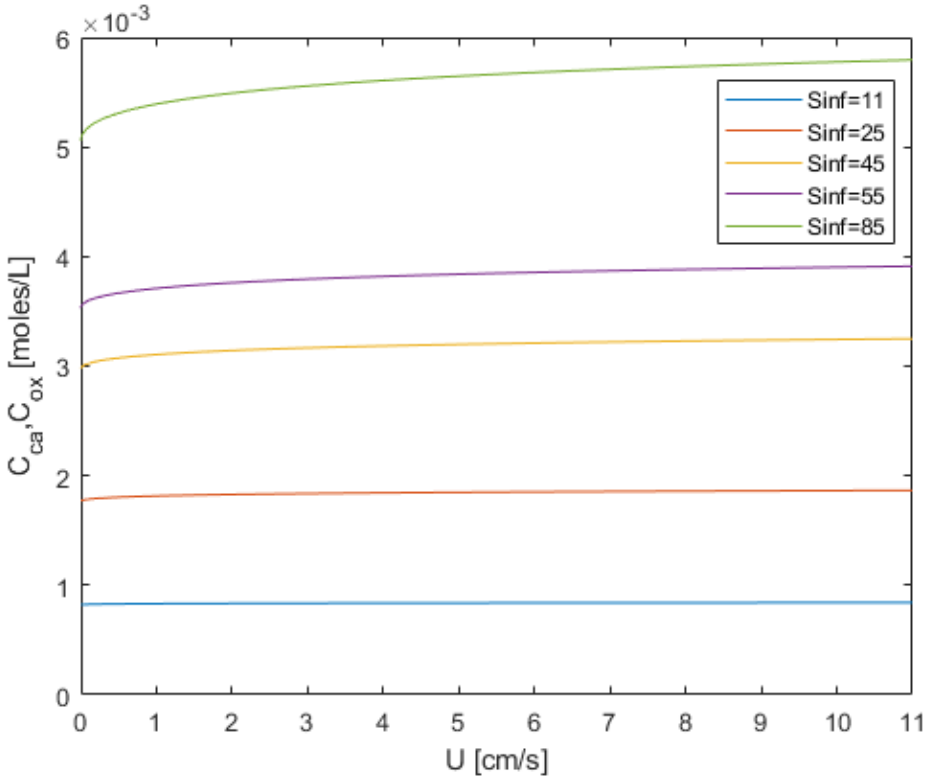

Figure 4.11: Effect of relative velocity U on the Ca and Ox surface concentration for different bulk solution supersaturations S_{inf} based on equal Ca and Ox solution concentration.

According to Eqn. 4.1 the change in growth rate is because of variations in the Ca and Ox surface concentration. In order to see what is happening around the CaOx particle, it is crucial to exam the effect of the relative velocity on the surface concentration of Ca and Ox for different supersaturation RS_{inf} as shown in Fig. 4.11. Ca and Ox surface concentrations at lower solution supersaturations are almost equivalent to the corresponding bulk concentration values in the solution. To provide a better overview, the impact of the Km (function of U, see Eqn. 4.8) on the Ca and Ox surface concentrations is displayed in Fig. 4.12. It is shown that the growth rate is controlled by the transport in the limit of small Km or U, especially at higher supersaturations the transport has more effect on the growth process. As expected, for slow transport process the rate of ions get onto the CaOx surface cannot keep up with the rate of ions consumed by the reaction on the CaOx surface. Thus, for large Km or U the Ca and Ox concentrations approach the bulk concentrations, the growth rate becomes independent of the transport process.

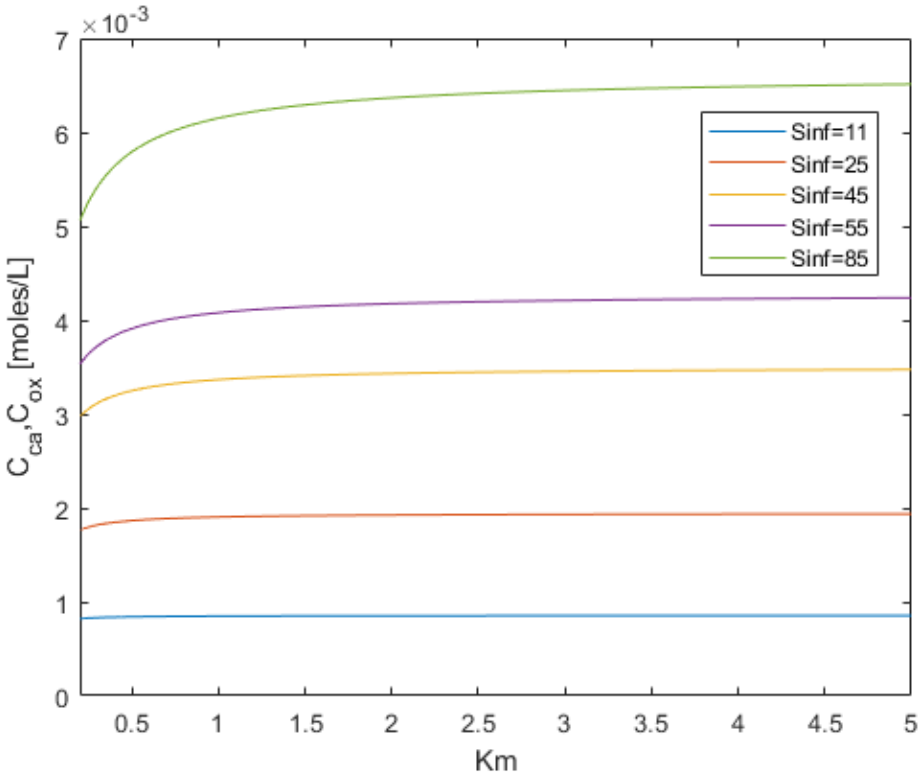

Figure 4.12: Effect of Km on the Ca and Ox surface concentration for different solution supersaturations RS_{inf} based on equal Ca and Ox solution concentration.

The reaction rate constant is dependent on urine chemical composition, the presence of inhibitors and promoters in the solution such as citrates, magnesium and alpha defensin etc. It is interesting to examine the influence of relative velocity on the CaOx growth rate at different reaction rate constant which varies from 0.2 to 2000 (L/mol)(cm/s) in Fig. 4.13. It shows that as the reaction rate constant increases, the CaOx growth rate becomes greater influenced by the relative velocity, especially when the reaction rate constant is at order of magnitude 10^3. Thus, at higher reaction rates, the CaOx growth rate is controlled by the transport. However, for lower reaction rates, where the crystallization is limited by the reaction, the CaOx growth rates are independent of transport.

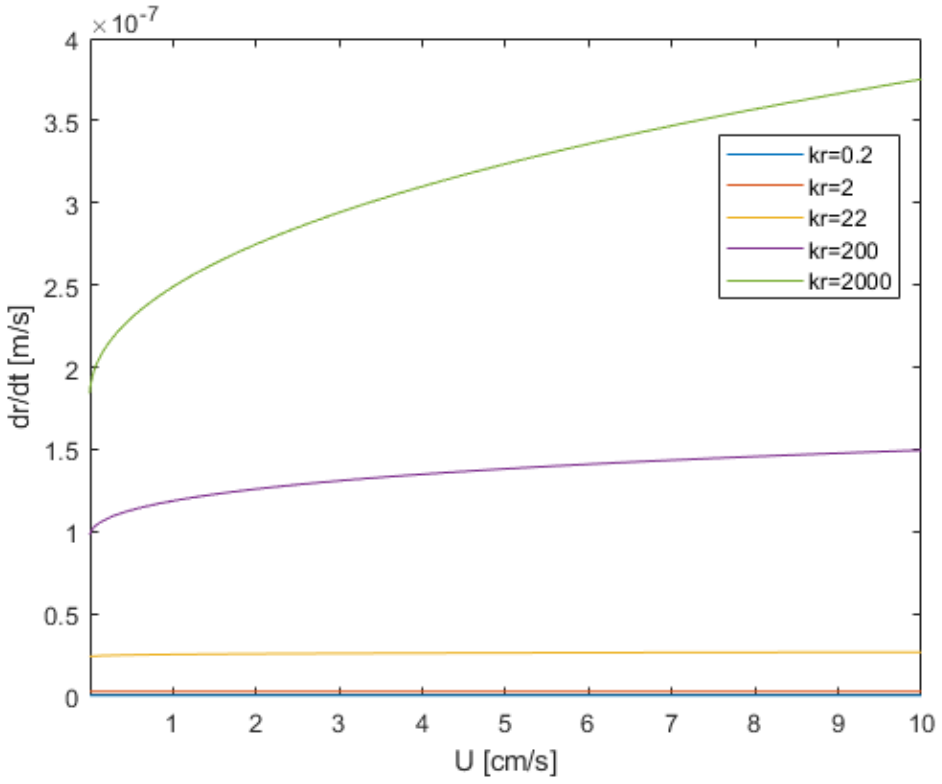

Figure 4.13: Effect of U on the CaOx growth rate for different surface reaction rate constant S_{inf} based on equal inlet solution concentration $C^*_{\infty,ca}$=$C^*_{\infty,ox}$=0.0039 (mol/L).

The relation between CaOx growth rate and the CaOx crystal radius for different relative velocities is shown in Fig. 4.14. The growth rate starts to decrease at a radius around 10^{-3} cm and decreases more as the crystal radius increases. The reason for this decrease can be explained by the fact that as the crystal radius gets bigger, ions needed by the reaction becomes incapable to be transported from the bulk to the larger surface areas of crystals. It is noted that for higher relative velocities, where the growth rate is more limited by the surface reaction, the growth rate starts to decrease at a bigger crystal radius in comparison with lower relative velocities. From Fig. 4.14 it can be seen that the growth rate is controlled by the surface reaction at around radius of 10^{-3} cm.

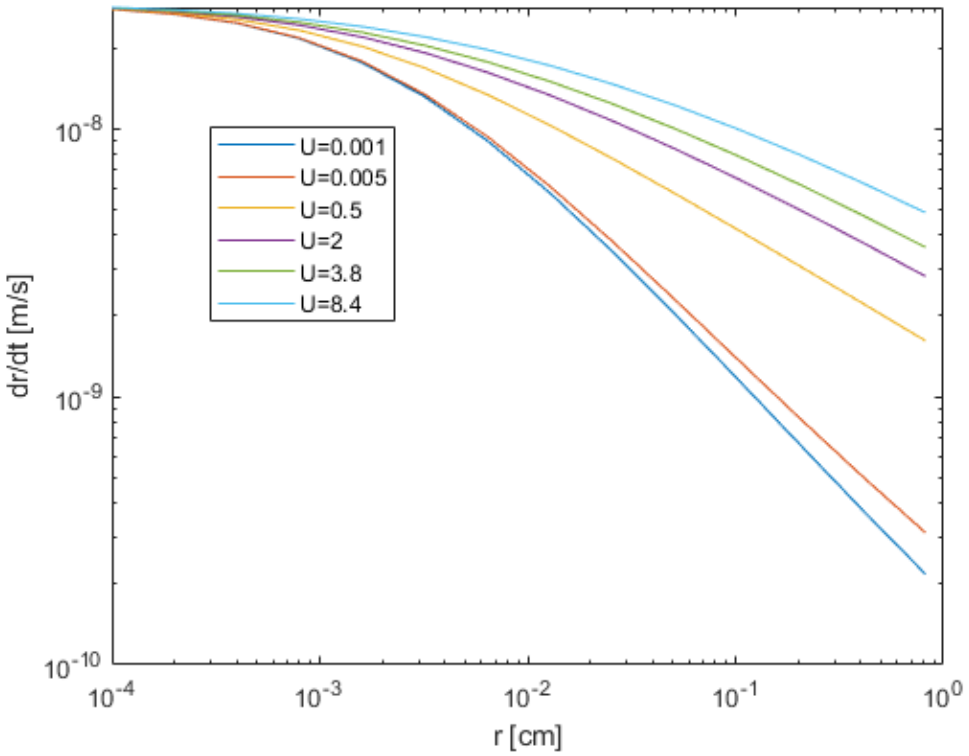

Figure 4.14: Effect of radius on the CaOx growth rate for different relative velocites with equal inlet solution concentration $C^*_{\infty,ca}$=$C^*_{\infty,ox}$=0.0039 (mol/L), K_r=22 (L/mol)(cm/s) and $S_{inf} = 25$.

4.2.2. Crystal growth of unequal Ca and Ox concentrations

In the previous experiments, equal molar Ca and Ox inlet concentrations were used for crystal growth study. In this section, the experiments were performed under hypercalciuria condition where the Ox inlet concentration is one thirtieth of the Ca inlet concentration.

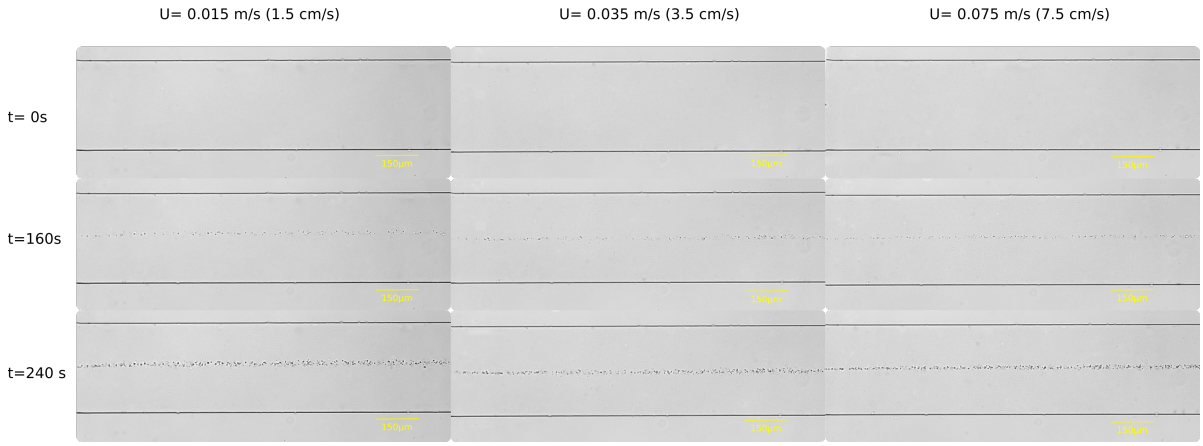

Figure 4.15: CaOx crystallization process inside the microchannel under 10x magnification under the Nikon microscope for different relative velocites with Ca inlet concentration= 0.012 M and Ox inlet concentrations= 0.0004 M.

The examination of CaOx particles was done by Nikon microscope at 10x magnification with the focus on the PDMS microchannel wall where the crystals are stationary (fixed). In Fig. 4.15 the CaOx crystal formation inside the microchannel at particular time step for different flow velocities is shown. CaOx crystal images were captured by Andor Zyla sCMOS camera and submitted to ImagJ for the analysis of the images, from which the surface area of each individual particles is extracted at two differet time steps. The radius of particle was calculated based on the particle area by assuming CaOx particle is to be spherical. In Table. 4.9 the average growth rate of crystal along with 95% confidence interval is reported.

Velocity (cm/s)	Velocity (m/s)	Growth rate (cm/min)	Growth rate (m/s)	95% Confidence interval (cm/min)	95% Confidence interval (m/s)
1.5	0.015	4.71×10^{-5}	7.85×10^{-9}	4.24×10^{-5}, 5.18×10^{-5}	7.07×10^{-9}, 8.63×10^{-9}
3.5	0.035	4.36×10^{-5}	7.27×10^{-9}	3.90×10^{-5}, 4.82×10^{-5}	6.50×10^{-9}, 8.03×10^{-9}
7.5	0.075	4.49×10^{-5}	7.48×10^{-9}	4.09×10^{-5}, 4.89×10^{-5}	6.82×10^{-9}, 8.15×10^{-9}

Table 4.9: Growth rate for different relative velocities with Ca inlet concentration= 0.012 M and Ox inlet concentration= 0.0004 M.

The results in Table. 4.9 show the influence of relative velocity is quite limited. A comparison between experimental data and modelling results for the CaOx growth rate in different relative velocities is presented in Fig. 4.16. Again, the physiochemical parameters in Table. 4.6 were applied. Qualitatively, these results indicated that the data obtained from the microfluidic experiments and modeling were highly consistent as same dependence pattern is observed as a function of velocity U. Quantitatively, both results show the magnitude of growth rate is in order of 10^{-9} m/s and the experimental obtained growth rate is higher than the modeling obtained growth rate.

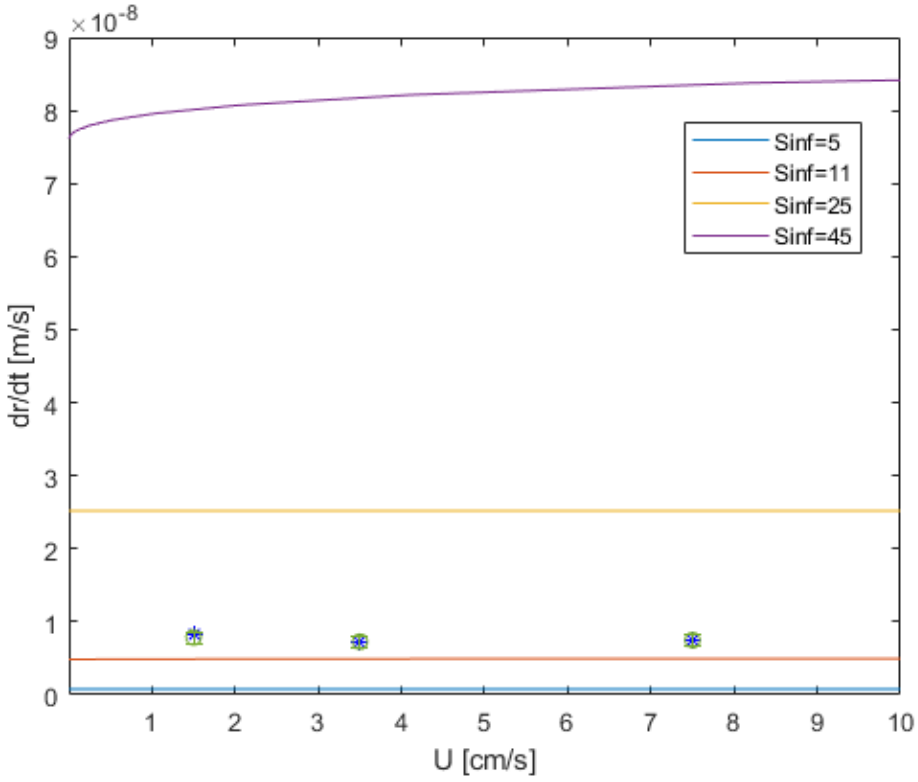

Figure 4.16: Effect of relative velocity U on the CaOx growth rate for different solution supersaturation based on $C^*_{\infty,ca}/C^*_{\infty,ox}$=30.

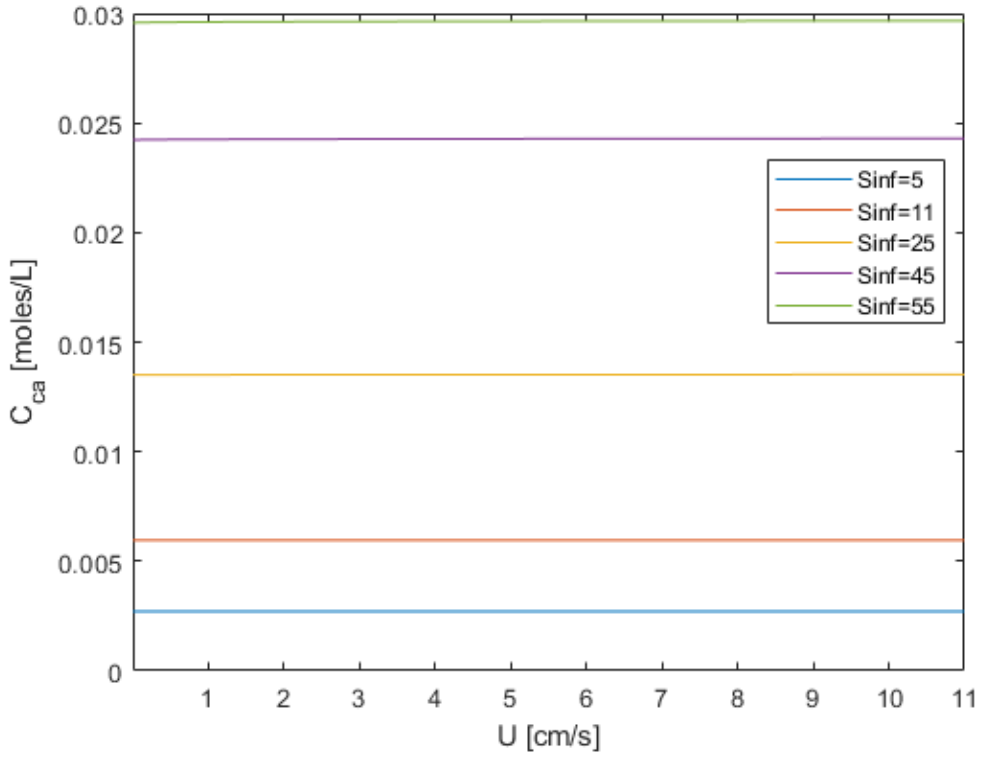

Figure 4.17: Effect of relative velocity U on the surface concentrations of Ca for different solution supersaturation R_{inf} based on $C^*_{\infty,ca}/C^*_{\infty,ox}$=30.

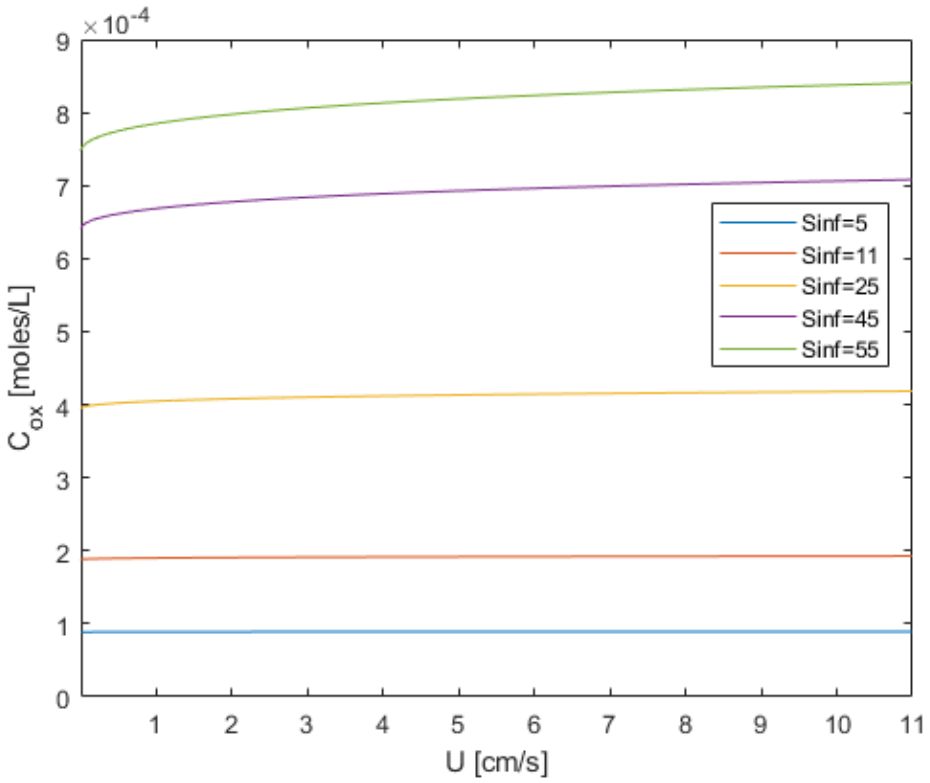

Figure 4.18: Effect of relative velocity U on the surface concentrations of Ox for different solution supersaturation based on $C^*_{\infty,ca}/C^*_{\infty,ox}$=30.

The effect of the relative velocity on the surface concentration of Ca and Ox for different supersaturation S_{inf} is shown in Fig.4.17 and Fig.4.18. These findings indicated the same patterns as observed in the equal molar concentration results. Fig.4.19 and Fig.4.20 show the surface concentration of Ca and Ox as a function of the relative velocity U for different surface reaction rate constants. When kr increases from 0.2 to 2000, the surface concentration of Ca was decreased with 2%, while that of Ox decreased with 80%. Thus, it is interesting to note that for unequal molar ionic concentrations, the crystal growth rate is more dependent on the ionic concentration of ion that is present in the lowest quantity in the bulk solution.

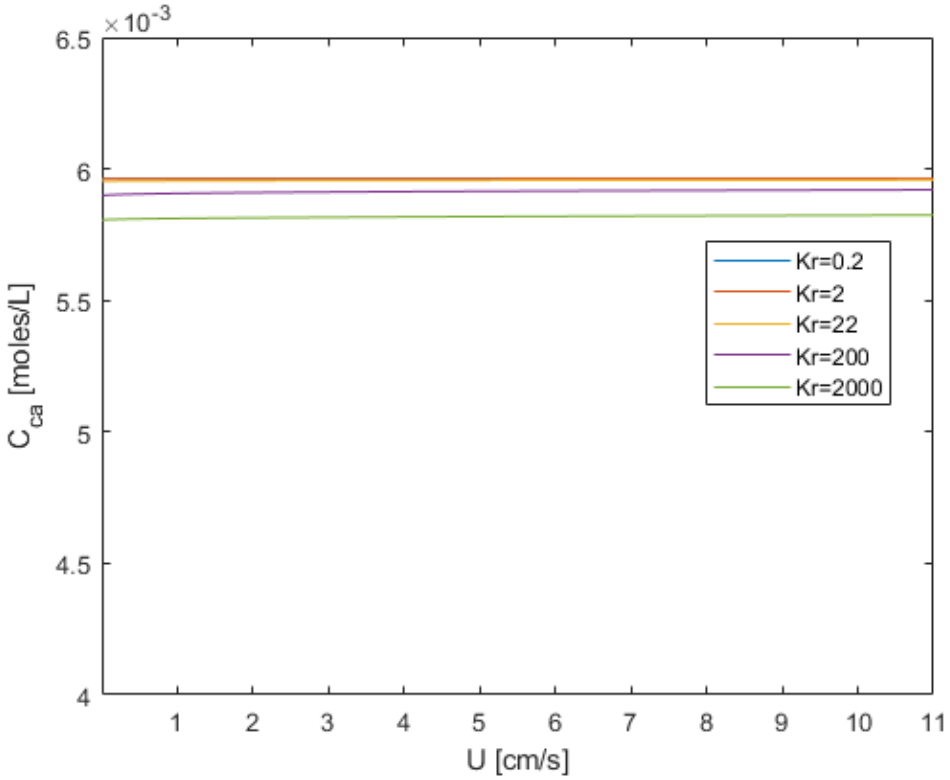

Figure 4.19: Effect of relative velocity U on the surface concentrations of Ca for different surface reaction rate constants Kr based on $C^*_{\infty,ca}/C^*_{\infty,ox}$=30 and S_{inf}= 11.

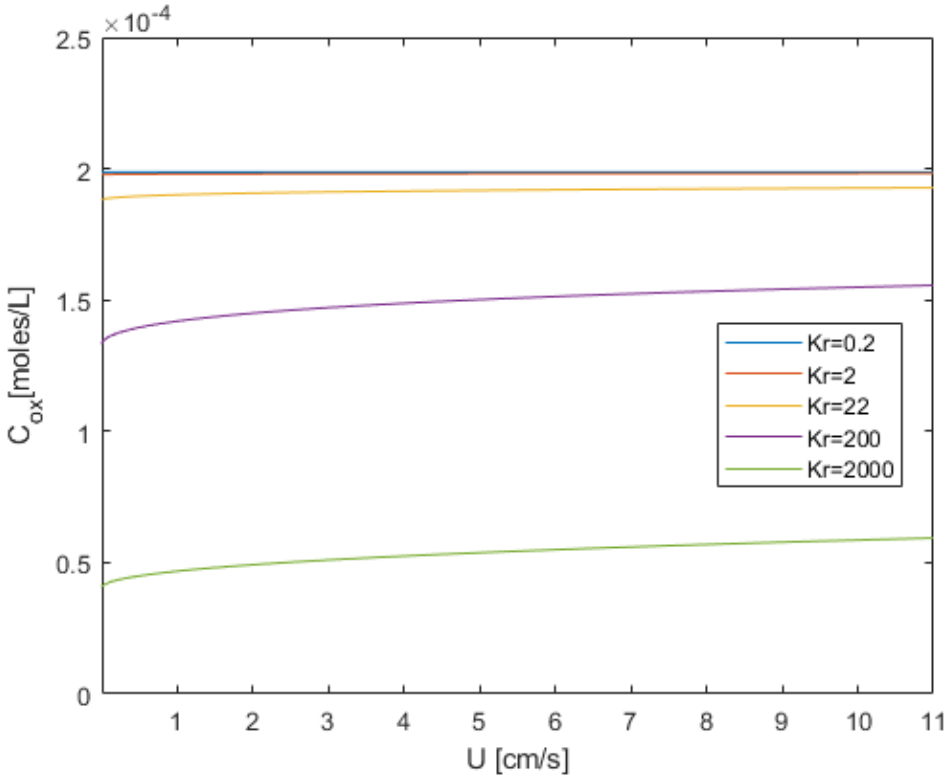

Figure 4.20: Effect of relative velocity U on the surface concentrations of Ox for different surface reaction rate constants Kr based on $C^*_{\infty,ca}/C^*_{\infty,ox}$=30 and S_{inf}=11.

The relation between CaOx growth rate and the crystal radius for different relative velocities is shown in Fig. 4.16. The results show the same trends observed in the equal molar bulk solution concentrations case. For the particle radius r smaller than 10^{-3} cm, the crystal growth rate is insensitive to the relative velocity U. It indicates that the growth rate is controlled by the surface reaction kinetics at particle radius around 10^{-3} cm.

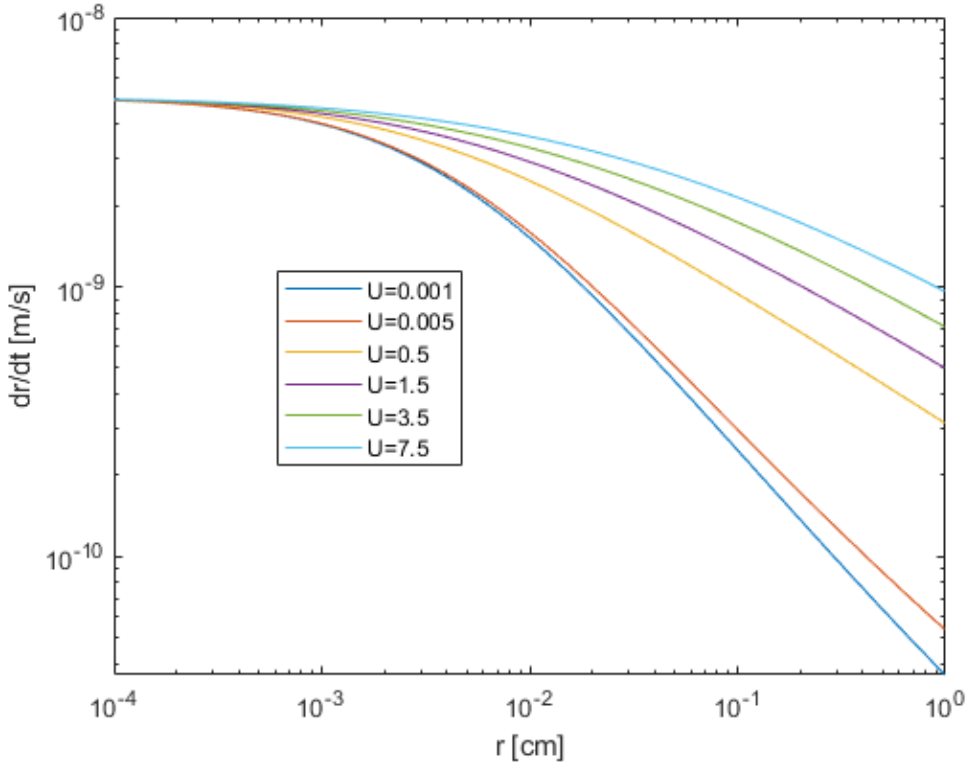

Figure 4.21: Effect of radius on the CaOx growth rate for different relative velocites based on $C^*_{\infty,ca}/C^*_{\infty,ox}$=30 and S_{inf}= 11, K_r=22 (L/mol)(cm/s).

4.2.3. Osteopontin

The inhibitor osteopontin (OPN) was chosen for study because it has been shown to decrease the formation and growth of calcium oxalate crystals [43]. OPN is a negatively charged acidic hydrophilic single-chain protein with a molecular weight of approximately 60 kDa [21]. The three OPN concentrations that have been tested under the same Ca and Ox bulk concentrations (0.012 M and 0.0004 M respectively) and relative velocity U=0.015 m/s (1.5 cm/s) were 1.44, 3.60 and 5.04 µg/mL. In Fig. 4.15 the CaOx crystal formation inside the microchannel at particular time step for OPN concentrations is shown.The results of growth rate were summarized in Table. 4.10.

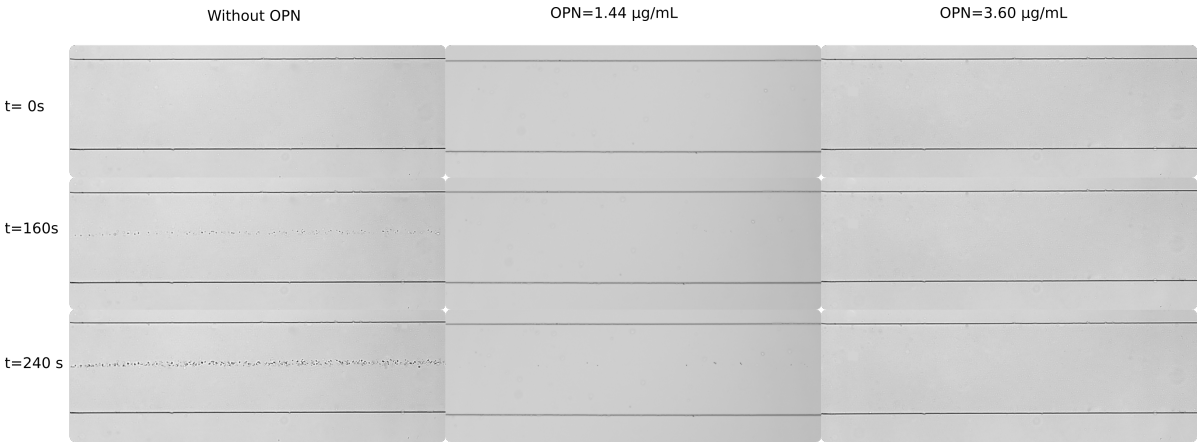

Figure 4.22: CaOx crystallization process inside the microchannel under 10x magnification under the Nikon microscope for different OPN concentrations at U= 0.015m/s (1.5 cm/s).

Molar ratio OPN: Ca ion	OPN in Ox stock solution (µg/mL)	Growth rate (cm/min)	Growth rate (m/s)	95% Confidence interval (cm/min)	95% Confidence interval (m/s)
2×10^{-6}	1.44	2.57×10^{-5}	4.28×10^{-9}	2.38×10^{-5}, 2.75×10^{-5}	3.97×10^{-9}, 4.58×10^{-9}
5×10^{-6}	3.6	1.26×10^{-5}	2.10×10^{-9}	1.14×10^{-5}, 1.38×10^{-5}	1.9×10^{-9}, 2.3×10^{-9}
7×10^{-6}	5.04	-	-	-	-

Table 4.10: Growth rates at different OPN concentrations with Ca=0.012 M and Ox=0.0004 M in the stock solutions

As expected, in the presence of OPN, the growth rate of calcium oxalate crystal was lower than the case where OPN is absent. The growth rate is a function of OPN concentration and obtain lower values at larger OPN concentration. For OPN concentration 5.04 µg/mL, no crystals were observed after 30 min. As the growth of calcium oxalate crystal occurs most rapidly at steps on hillocks generated from screw dislocations, it is believed that OPN is adsorbed to these growth steps [40]. A large number of carboxylic acid of OPN will strongly bind the steps, leading to step pinning, modification of step kinetics and as a result the growth rate is inhibited [29].

In all the above cases, the supersaturation at the centre-line was assumed to be remained virtually constant for a while. However, it should be noted that the assumption of constant supersaturation declines in validity.

5

Conclusion and Recommondations

5.1. Conclusion

5.1.1. Supersaturation simulation using CFD tools

The main goal of this research is to study the growth rate of CaOx crystal at different relative velocities and ionic specie concentrations. The first step was to structure a 3D model of the microchannel used in the experiment with ANSYS/Fluent CFD code. In this simulation, the flow dynamics and mass transfer were combined to determine the supersaturation profile in the microchannel for different constant flow rates and Ca and Ox inlet concentrations. It was found that the maximum supersaturation is reached near the centre of the microchannel at position y ≈-1 μm and the maximum supersaturation value was half of the inlet ionic concentrations. The results showed that the supersaturation values at x= 500 μm and 6 μm away from the interface in y-direction deviate negligibly from the maximum value. Thus, for the microfluidic CaOx growth rate experiments the crystal particles in the region $y_{interface} \pm \Delta y$, x >500 μm were analysed for the size measurement.

5.1.2. Calcium Oxalate Crystal Growth

In this study, a PDMS microfluidic channel was used to mimic the collecting duct in kidney. The crystal growth rate measurements were measured with a aid of an optical microscope, which provided a continuous observation of growth during the entire experiment. The experiments were conducted in an equal molar ionic concentration condition where Ca and Ox inlet concentrations= 0.0039 M and in an unequal molar concentration condition where Ca inlet concentration= 0.012 M and Ox inlet concentration= 0.0004 M. Qualitatively, the data obtained from experiments and the modelling results were highly consistent. Quantitively, the experimental obtained growth rate is higher than the modelling growth rate. It was shown that the crystal growth rate increases with solution supersaturation increasing and decreases with the crystal size increasing. The findings also indicated that under conditions

of low bulk solution supersaturation and low surface reaction constant values, the growth rates are controlled by the surface reaction kinetics and independent of the species transport. When the bulk solution supersaturation and surface reaction constant values are high, the Ca and Ox surface concentrations become lower than their bulk solution values and the crystal growth rates are controlled by the species transport. It was also shown that in the presence of inhibitor osteopontin, the crystal growth rate was decreased. For osteopontin concentration 5.04 µg/ml, there was no sign of crystals after 30 min.

5.2. Recommendations

- It is recommended to perform all the preparation and semi-curing steps in a dust free working environment to limit the impurities inside the microchannel. By increasing the chance of success of making usable microfluidic device will reduce the workload and save time.
- It is advised to perform this study with other different Ca and Ox inlet concentrations and compare the experimental results with the modelling obtained results.
- The physiological conditions in the collecting duct can be better mimicked by using artificial urine. It is suggested to perform the experiments under artificial urine condition.
- In the current CFD simulation, the precipitation reaction between Ca and Ox is not yet incorporated. To obtain supersaturation profile with higher accuracy, PBE model could be coupled to a CFD model using an Eulerian approach.
- In order to have a constant flow rate during the experiment, the flow rate controller can be used.

A

Supersaturation curves

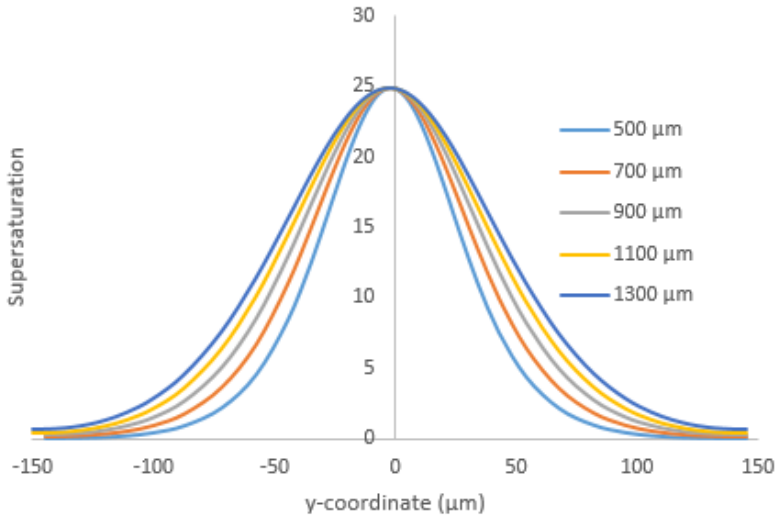

Figure A.1: The variation in supersaturation with y-coordinate for different x width position of the microchannel at z=8.5 μm for Ca inlet concentration=0.0039 M, Ox inlet concentration=0.0039 M, flow rate= 2.7 $\times$ 10^{-10} m^3/s, mean velocity=0.020 m/s (2.0 cm/s).

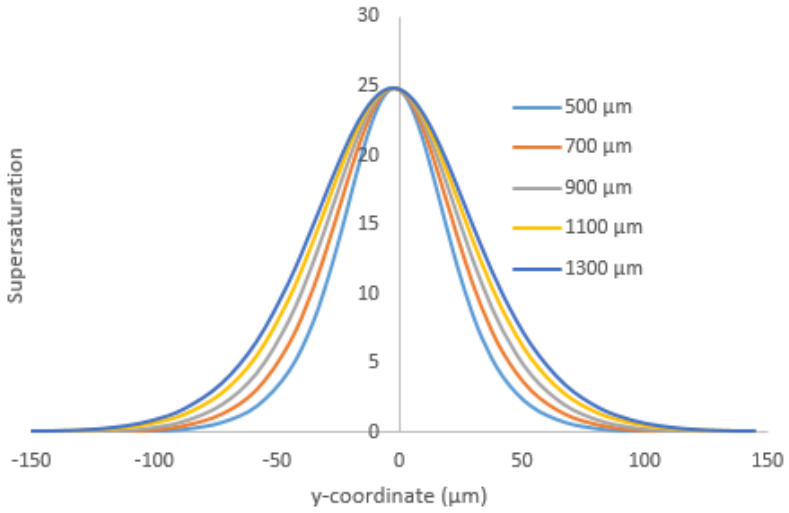

Figure A.2: The variation in supersaturation with y-coordinate for different x width position of the microchannel at z=8.5 μm for Ca inlet concentration=0.0039 M, Ox inlet concentration=0.0039 M, flow rate= 5.0 $\times 10^{-10}\ m^3/s$, mean velocity=0.038 m/s (3.8 cm/s).

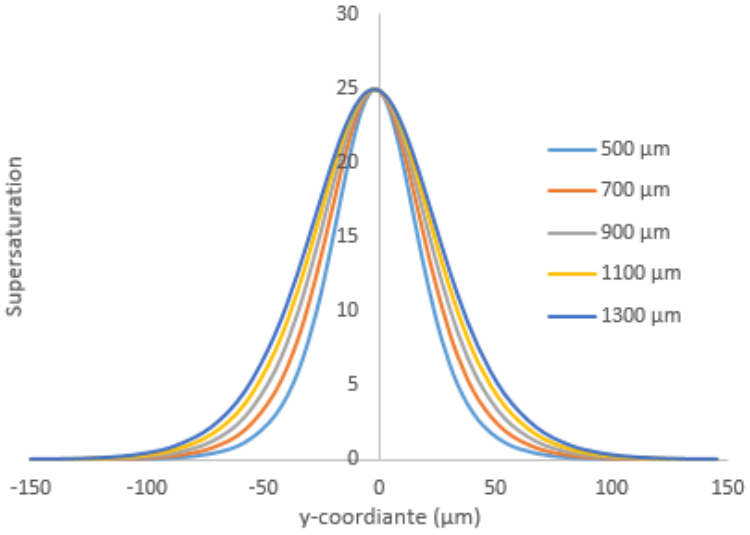

Figure A.3: The variation in supersaturation with y-coordinate for different x width position of the microchannel at z=8.5 μm for Ca inlet concentration=0.0039 M, Ox inlet concentration=0.0039 M, flow rate= 7.0 $\times 10^{-10}\ m^3/s$, mean velocity=0.070 m/s (7.0 cm/s).

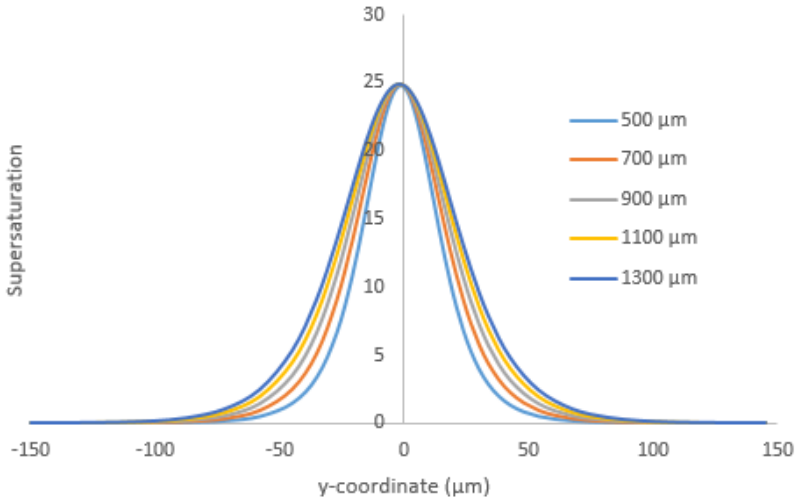

Figure A.4: The variation in supersaturation with y-coordinate for different x width position of the microchannel at z=8.5 μm for Ca inlet concentration=0.0039 M, Ox inlet concentration=0.0039 M, flow rate= 1.1 $\times 10^{-9}\ m^3/s$, mean velocity=0.084 m/s (8.4 cm/s).

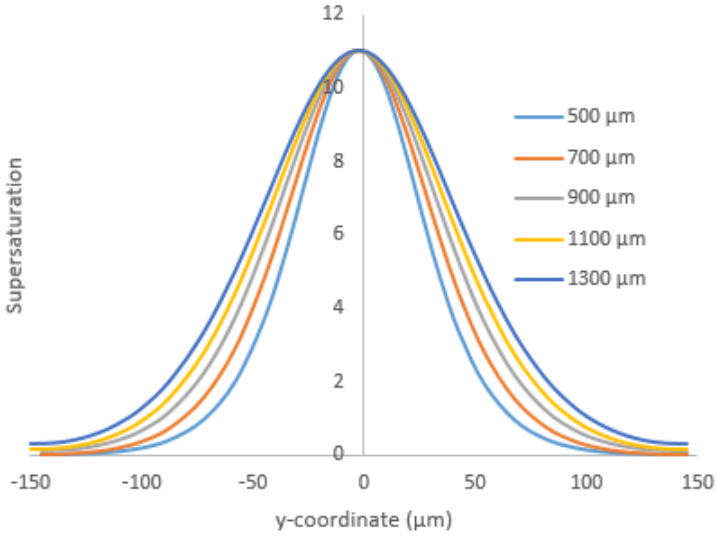

Figure A.5: The variation in supersaturation with y-coordinate for different x width position of the microchannel at z=8.5 μm for Ca inlet concentration=0.012 M, Ox inlet concentration=0.0004 M, flow rate= 2.0 $\times 10^{-10}\ m^3/s$, mean velocity=0.015 m/s (1.5 cm/s).

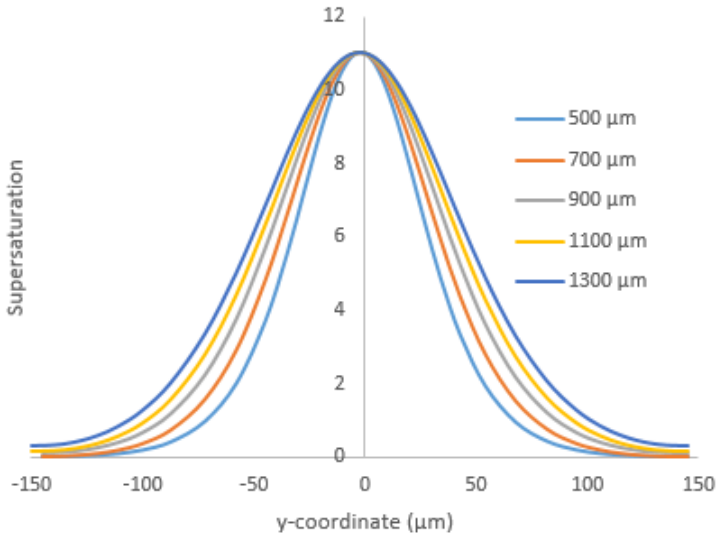

Figure A.6: The variation in supersaturation with y-coordinate for different x width position of the microchannel at z=8.5 μm for Ca inlet concentration=0.012 M, Ox inlet concentration=0.0004 M, flow rate= 4.6 $\times$ 10^{-10} m^3/s, mean velocity=0.035 m/s (3.5 cm/s).

B

Experimental setup

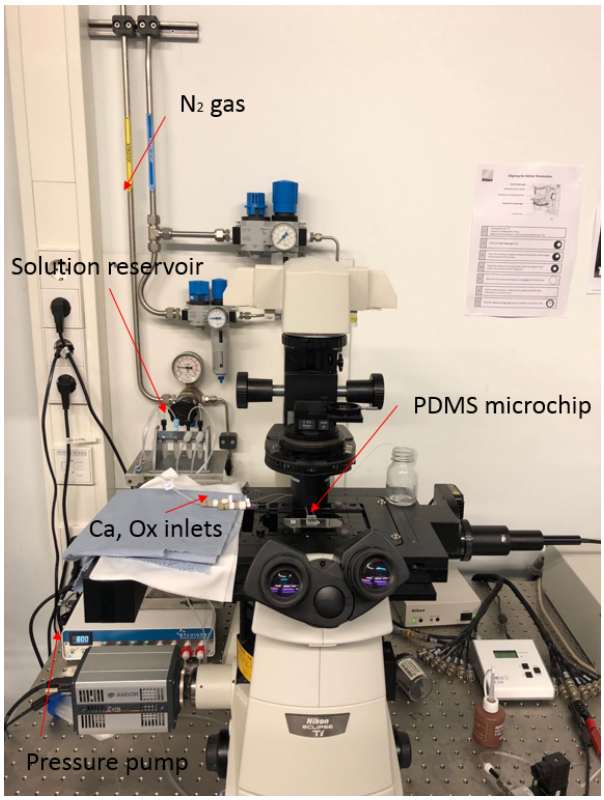

Figure B.1: The CaOx crystal growth microfluidic experimental setup

C

Growth Rate

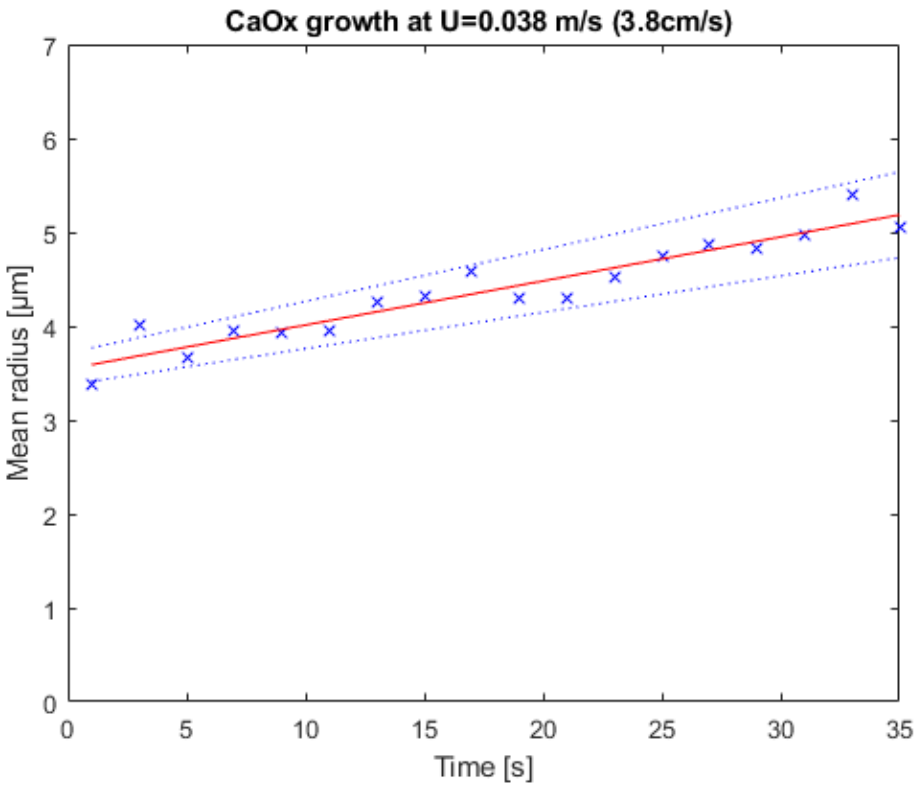

Figure C.1: CaOx mean radius vs time for relative velocity U=0.038 m/s (3.8 cm/s) with equal inlet solution concentration $C^*_{\infty,ca}$=$C^*_{\infty,ox}$=0.0039 (mol/L)

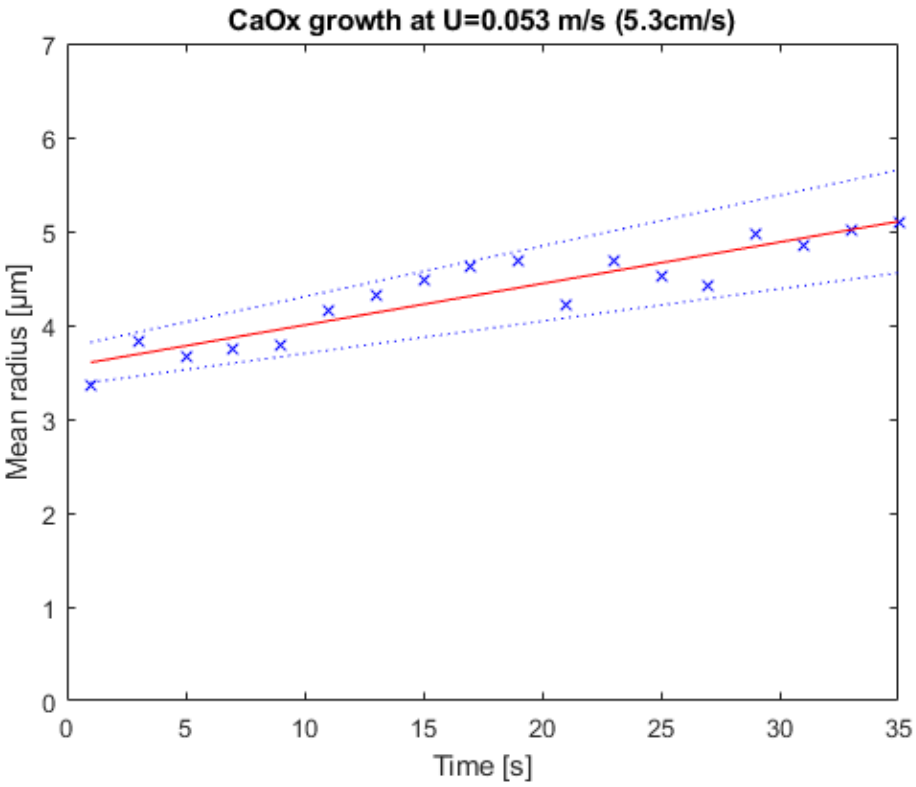

Figure C.2: CaOx mean radius vs time for relative velocity U=0.053 m/s (5.3 cm/s) with equal inlet solution concentration $C^*_{\infty,ca}$=$C^*_{\infty,ox}$=0.0039 (mol/L)

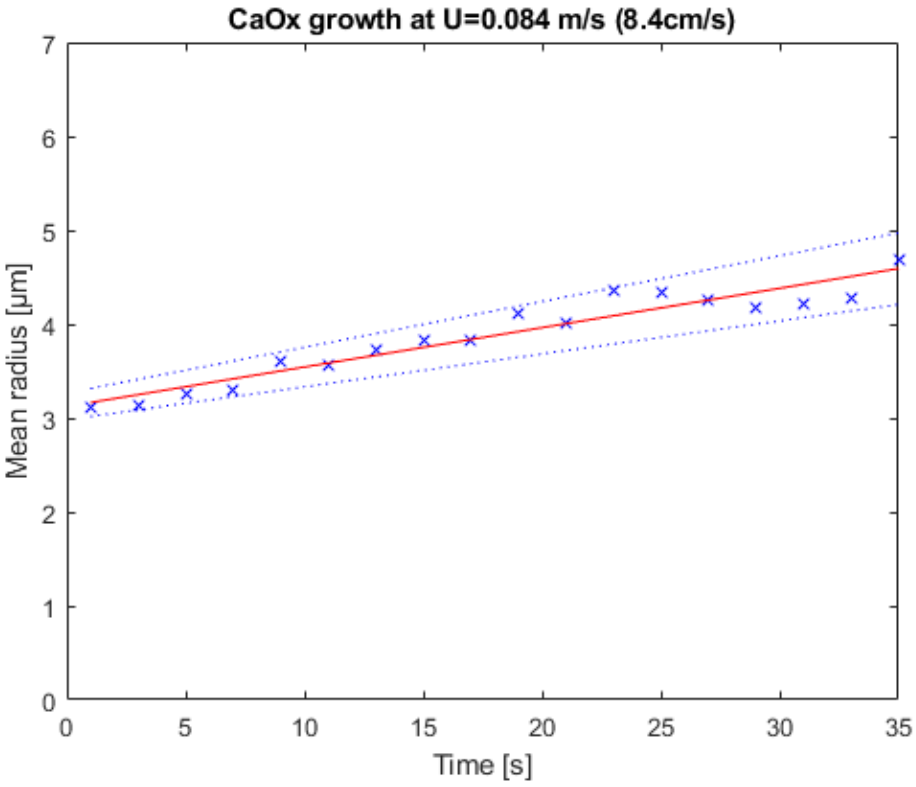

Figure C.3: CaOx mean radius vs time for relative velocity U=0.084 m/s (8.4 cm/s) with equal inlet solution concentration $C^*_{\infty,ca}$=$C^*_{\infty,ox}$=0.0039 (mol/L)

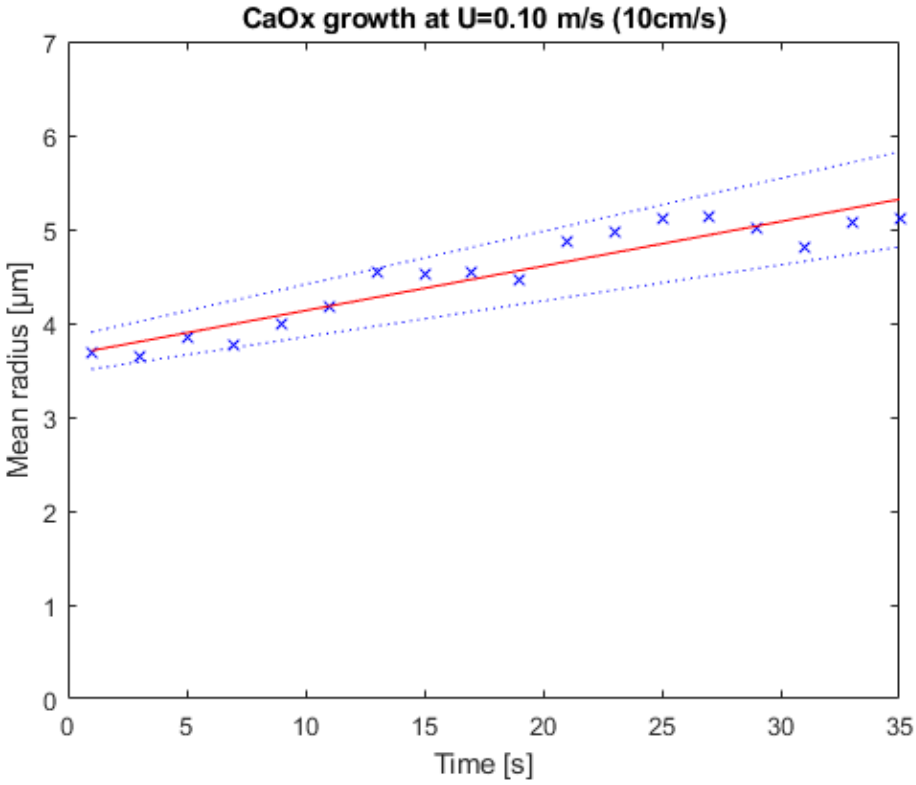

Figure C.4: CaOx mean radius vs time for relative velocity U=0.01 m/s (10 cm/s) with equal inlet solution concentration $C^*_{\infty,ca}$=$C^*_{\infty,ox}$=0.0039 (mol/L)

Bibliography

[1] A.Bensatal and M.R.Ouahrani. Inhibition of crystallization of calcium oxalate by the extraction of Tamarix gallica Lo Title. *Urological Research*, 36(6):283–287, 2008.

[2] A.E.Neilsen. Transport control in crystal growth from solution. *CCACCA*, 53(2):255–279, 1980.

[3] A.W.Vere. *Crystal Growth: Principles and Progress*. Springer Science & Business Media, 1st edition, 2013. ISBN 978-1-4757-9899-9. doi: 10.1007/978-1-4757-9897-5.

[4] Frank FC. Burton WK, Cabrera N. The growth of crystals and the equilibrium structure of their surfaces. *Philosophical Transactions of the Royal Society A-Mathematical Physical and Engineering Sciences*, 243:299–358, 1951.

[5] D. R. Basavaraj, C. S. Biyani, A. J. Browning, , and J. J. Cartledge. Te role of urinary kidney stone inhibitors and promoters in the pathogenesis of calcium containing renal stones. *EAU-EBU Update Series*, 5(3):126–136, 2007.

[6] et al Ming NB, Tsukamoto K, Sunagawa I. Stacking faults as self-perpetuating step sources. *Journal of Crystal Growth*, 91 (1):11–19, 1988.

[7] A. P. Evan. Physiopathology and etiology of stone formation in the kidney and the urinary tract. *Pediatric Nephrology*, 25(5):931–841, 2010.

[8] B. Finlayson and F. Reid. The expectation of free and fixed particles in urinary stone disease, 1978. ISSN 00210005.

[9] Fluigent. Pressure Control Technologies. URL https://www.fluigent.com/pressure-control-technologies/.

[10] G.L. Gardner. Nucleation and crystal growth of calcium oxalate trihydrate. *Journal of Crystal Growth*, 30(158), 1975.

[11] O. Garside, J.; Sohnel. *Precipitation: Basic Principles and Industrial Applications*. Butterworth-Heinemann, 1st edition, 1993. ISBN 978-0750611077.

[12] Arunachalam Ramanan Gautam R Desiraju, Jagadese J Vittal. *Crystal Engineering A Textbook*. World Scientific Publishing, 1st edition, 2011. ISBN 13 978-981-4338-75-2.

[13] G.H.Nancollas. Crystallization theory relating to urinary stone formation. *World Journal of Urology*, 1(3):131–137, 1983. ISSN 07244983.

[14] Robert S. Brodkey□ Harry C. Hershey. *Transport Phenomena: A Unified Approach*. Brodkey Publishing, 1st edition, 2003. ISBN 0972663592.

[15] J. M. Teichman and M. H. Joel. Acute renal colic from ureteral calculus. *European Urology Supplements*, 9(7):802–806, 2010.

[16] Ernest J. Henley J.D.Seader. *Separation Process Principles*. John Wiley & Sons, 2nd edition, 2006. ISBN 13-978-0-471-46480-8.

[17] M.Broul J.Nyvlt, O.Sohnel, M.Matuchova. *The Kinetics of Industrial crystallizaiton*. Elsevier Science, New York, 1st edition, 1985. ISBN 0-444-41295-6.

[18] Nikola Kallay. *Interfacial Dynamics*. CRC Press, 1st edition, 2000. ISBN 9781482289794.

[19] Mohammad Kassemi, Robert Brock, and Noel Nemeth. A combined transport-kinetics model for the growth of renal calculi. *Journal of Crystal Growth*, 332(1):48–57, 2011. ISSN 00220248. doi: 10.1016/j.jcrysgro.2011.07.009. URL http://dx.doi.org/10.1016/j.jcrysgro.2011.07.009.

[20] K. K. Malhotra. Medical aspects of renal stones: review. *Journal of Indian Academy of Clinical Medicine*, 9(4):282–286, 2008.

[21] M. Mazzali, T. Kipari, V. Ophascharoensuk, J. A. Wesson, R. Johnson, and J. Hughes. Osteopontin-A molecule for all seasons. *QJM - Monthly Journal of the Association of Physicians*, 95(1):3–13, 2002. ISSN 14602725. doi: 10.1093/qjmed/95.1.3.

[22] John L. Meyer and Lynwood H. Smith. Growth of calcium oxalate crystals. I. A model for urinary stone growth, 1975. ISSN 00210005.

[23] G.H.Nancollas M.Sheehan. Calcium oxalate crystal growth: a new constant composition method for modeling urinary stone formation. *Invest.Urol*, 17(6):446–450, 1980.

[24] G. H. Nancollas. Crystallization theory relating to urinary stone formation. *World Journal of Urology*, 1(3):131–137, 1983. ISSN 07244983. doi: 10.1007/BF00326900.

[25] Arne E. Nielsen. Theory of electrolyte crystal growth the parabolic rate law. *Pure and Applied Chemistry*, 53(11):2025–2039, 1981. ISSN 13653075. doi: 10.1351/pac198153112025.

[26] Glenn M. Preminger John P., Nagaraja P. Rao. *Urinary Tract Stone Disease*. Springer Science & Business Media, 1st edition, 2011.

[27] Jukka Peter Kleinebudde, Johannes Khinast. *Continuous Manufacturing of Pharmaceuticals*. John Wiley & Sons, 1st edition, 2017.

[28] James Keeler Peter William Atkins, Julio De Paula. *Atkins' Physical Chemistry*. Oxford University Press, 11 edition, 2018.

[29] S. R. Qiu, A. Wierzbicki, C. A. Orme, A. M. Cody, J. R. Hoyer, G. H. Nancollas, S. Zepeda, and J. J. De Yoreo. Molecular modulation of calcium oxalate crystallization by osteopontin and citrate. *Proceedings of the National Academy of Sciences of the United States of America*, 101(7):1811–1815, 2004. ISSN 00278424. doi: 10.1073/pnas.0307900100.

[30] Alan G. Wasserstein Raven Goel. Kidney Stones: Diagnostic and Treatment Strategies. *Consultant*, 52(2), 2012.

[31] R.Marc. Z.physik. Chem. *Z.physik. Chem*, 61:385–398, 1908.

[32] Naír Rodríguez-Hornedo and Denette Murphy. Significance of controlling crystallization mechanisms and kinetics in pharmaceutical systems. *Journal of Pharmaceutical Sciences*, 88(7):651–660, 1999. ISSN 00223549. doi: 10.1021/js980490h.

[33] E. Rosseeva, O. Frank-Kamenetskaya, Dmitrii Vlasov, Marina Zelenskaya, Katerina Sazanova, Aleksei Rusakov, and R. Kniep. Crystallization of calcium oxalate hydrates by interaction of calcite marble with fungus aspergillus niger. *American Mineralogist*, 100:2559–2565, 11 2015. doi: 10.2138/am-2015-5104.

[34] Ronald W. Rousseau. *Handbook of Separation Process Technology*. Sons, John Wiley, 1st edition, 1987. ISBN 047189558X.

[35] Nakajima K Sato K, Furukawa Y. *Advances in Crystal Growth Research*. Elsevier Science, 2001.

[36] Ehsan Shabani, Mohammad J Abdekhodaie, and Seyyed Abbas Mousavi. Modeling of Calcium Oxalate Kidney Stone Growth. pages 109–112, 2018. doi: 10.17758/eares1.eap0518139.

[37] Xiaoxia Sheng, Michael D. Ward, and Jeffrey A. Wesson. Crystal surface adhesion explains the pathological activity of calcium oxalate hydrates in kidney stone formation. *Journal of the American Society of Nephrology*, 16(7):1904–1908, 2005. ISSN 10466673.

[38] A. Malthe Sørenssen. *Chemical potential and Gibbs Distribution*. 2013.

[39] L. Giannossi Summa and V. *A review of pathological bio-mineral analysis techniques and classification schemes, in An Introduction to the Study of Mineralogy*. C. Aydinalp, Ed., InTechOpen, InTech, IMAA-CN„ Italy, 2012.

[40] Michael D Ward Taesung Jung, Xiaoxia Sheng, Chang Kyun Choi, Woo-Sik Kim, Jeffrey A Wesson. Probing crystallization of calcium oxalate monohydrate and the role of macromolecule additives with in situ atomic force microscopy. *Langmuir*, 20(20):8587–8596, 2004.

[41] Verschuren CA, Leys MR, Marschner T. A modified BCF model to quantitatively describe the (100) InP growth rate in chemical beam epitaxy. *Journal of Crystal Growth*, 188(1-4):11–16, 1998.

[42] Jr. William D. Callister. *Materials Science and Engineering An Introduction*. John Wiley & Sons, 7th edition, 2007. ISBN 978-0-471-73696-7.

[43] A. M. Worcester, E. M. Beshensky. Osteopontin Inhibits Nucleation of Calcium Oxalate Crystals. *Annals of the New York Academy of Sciences*, 760:375–377, 1995.